Final Technical Report on FA5209-05-P-0104 (AOARD-04-4075)

Investigation of excitonic polaritons in ZnO microcavities

Principal Investigator:
Shigefusa Chichibu, Dr. Eng. (Professor)
Institute of Applied Physics, University of Tsukuba
1-1-1 Tennodai, Tsukuba, Ibaraki 305-8573, Japan
Area Code/Phone Number: +81-29-853-5289 Fax Number: +81-29-853-5205
E-mail: chichibu@bk.tsukuba.ac.jp
Co-Principal Investigators:
Prof. Dr. Takayuki Sota (Waseda University, Tokyo, Japan)
Dr. Takeyoshi Onuma (University of Tsukuba)

Contents

Report Documentation Page

Form Approved
OMB No. 0704-0188

1. REPORT DATE	2. REPORT TYPE	3. DATES COVERED
28 JUL 2006	**Final Report (Technical)**	**05-11-2004 to 05-01-2006**

4. TITLE AND SUBTITLE	5a. CONTRACT NUMBER
Investigation of excitonic polaritons in ZnO microcavities	**FA520905P0104**
	5b. GRANT NUMBER
	5c. PROGRAM ELEMENT NUMBER
6. AUTHOR(S)	5d. PROJECT NUMBER
Shigefusa Chichibu	5e. TASK NUMBER
	5f. WORK UNIT NUMBER
7. PERFORMING ORGANIZATION NAME(S) AND ADDRESS(ES)	8. PERFORMING ORGANIZATION REPORT NUMBER
University of Tsukuba, Institute of Applied Physics,1-1-1 Tennodai,Tsukuba, Ibaraki 305-8573,Japan,JP,305-8573	**AOARD-054009**
9. SPONSORING/MONITORING AGENCY NAME(S) AND ADDRESS(ES)	10. SPONSOR/MONITOR'S ACRONYM(S)
The US Resarch Labolatory, AOARD/AFOSR, Unit 45002, APO, AP, 96337-5002	**AOARD/AFOSR**
	11. SPONSOR/MONITOR'S REPORT NUMBER(S) **AOARD-054009**

12. DISTRIBUTION/AVAILABILITY STATEMENT
Approved for public release; distribution unlimited

13. SUPPLEMENTARY NOTES

14. ABSTRACT

Cavity-coupled excitonic polaritons in ZnO microcavities is observed. The cavity is composed of ZnO wavelength (l)-cavity and high reflectivity distributed Bragg reflectors (DBRs). DBRs was composed of p-AlGaN/GaN, n-MgxZn1-xO/MgyZn1-yO, or SiO2/ZrO2 multiple quarter-wavelength (l/4) layers, and is also studied for future realization of threshold-free coherent light source that relies on Bose-Einstein condensation of cavity exciton-polaritons. Also, fundamental study of recombination mechanisms of excitonic polaritons in ZnO is also investigated. Fabrication and characterization of pn devices are planned to be carried out when strong coupling between exciton polaritons and cavity modes occur.

15. SUBJECT TERMS
Photoluminescence, Semiconductor Characterization, Zinc Oxide

16. SECURITY CLASSIFICATION OF:			17. LIMITATION OF ABSTRACT	18. NUMBER OF PAGES	19a. NAME OF RESPONSIBLE PERSON
a. REPORT	b. ABSTRACT	c. THIS PAGE			
unclassified	**unclassified**	**unclassified**		**44**	

A Statement of Work Approved

Final Goal:

To observe cavity-coupled [1] excitonic polaritons in ZnO microcavities composed of ZnO wavelength (λ)-cavity and high reflectivity distributed Bragg reflectors (DBRs) composed of p-AlGaN/GaN, n-$Mg_xZn_{1-x}O$/$Mg_yZn_{1-y}O$, or SiO_2/ZrO_2 multiple quarter-wavelength (λ/4) layers for future realization of threshold-free coherent light source [2] relying on Bose-Einstein condensation of cavity exciton-polaritons. Also, to obtain fundamental understandings for recombination mechanisms of excitonic polaritons in ZnO. Fabrication and characterization of p-n devices will be carried out if we succeed to observe strong coupling regime between exciton polaritons and cavity modes.

Objectives:

(1) Growth of ZnO and MgZnO epilayers by the unique epitaxial growth technique called *helicon-wave-excited-plasma sputtering epitaxy* (HWPSE) method [3].
(2) Determination of exact energies of longitudinal and transverse excitons in polar (0001) and nonpolar (11-20) ZnO epilayers.
(3) Characterization of the epilayers using time-resolved photoluminescence (TRPL), photoluminescence excitation, photovoltaic, and transmittance measurements and by modulation spectroscopy like electroreflectance (ER) and photoreflectance (PR) measurements [4].
(4) Study of cavity-coupled excitonic polaritons of ZnO microcavities combined with ZnO and high reflectivity distributed Bragg reflectors (DBRs) composed of p-AlGaN/GaN, n-$Mg_xZn_{1-x}O$ / $Mg_yZn_{1-y}O$, or SiO_2/ZrO_2 multiple λ/4 layers.

B Milestones and Deliverables Originally Planned

Followings are the original plan of this work.

(i) First quarter (Dec. 2004-Feb. 2005)

To grow ZnO and MgZnO alloy single epilayers using a newly settled HWPSE equipment. Since it has a load-lock system, we will be able to improve each epilayer quality. Deposition of SiO_2 and ZrO_2 by both e-beam (EB) evaporation and HWPS methods. Reactive HWPS will be carried out to deposit those dielectric insulating films. Growth of AlN on GaN/sapphire templates using NH_3-MBE will also be carried out.

(ii) Second quarter (Mar. 2005- May 2005)

To fabricate SiO_2 / ZrO_2 DBR by EB evaporation, in order to tune the central wavelength and reflectivity stop band of the mirror. We have fabricated three-source EB system, and we can deposit those. Simultaneously, tuning of SiO_2 and ZrO_2 deposition by HWPS will be carried out.

To grow good quality ZnO and MgZnO epilayers using appropriate interlayers (buffer layers) on the (11-20) sapphire substrates. Since the new HWPSE machine has multi-target holder by which 4 targets can be used without the growth interruption, heterostructures will be grown.

To fabricate AlN/AlGaN heterostructures by NH_3-MBE. These heterostructures will be used for the high-reflectivity mirror for the excitonic polariton lasers.

(iii) Third quarter (Jun. 2005- Aug. 2005)

To tune the deposition conditions for the best dielectric DBR by EB evaporation and HWPS

methods. We will use a combinatorial approach to optimize the structure.

To grow ZnO/MgZnO heterostructures on the buffer layers. These epitaxial structures will be looked at by TRPL and positron annihilation methods. Determination of the excitonic polariton energies will be carried out.

By using these dielectric and MgZnO/MgZnO or AlN/AlGaN DBRs, test structure of the ZnO λ-cavity will be prepared. Then measure the reflectivity as a function of the incidence angle.

(iv) Final quarter (Sep. 2005- Nov. 2005)

Fabrication of the λ-cavity to observe cavity-coupled excitonic polaritons. All considerable structures will be looked at by temperature-dependent reflectivity measurements to see the strong-coupling regime in ZnO. Thinning of the ZnO epilayer will be carried out using a sort of combinatorial method for the quick optimization of the structure. Final report will be submitted by the end of December.

C Summary of the results (Dec. 2004-Nov. 2005)

(1) HWPSE of ZnO and MgZnO

We eventually observed excitonic polariton emissions originating from transverse and longitudinal free A- and B-excitons at 9 K from ZnO epilayers grown at 750 °C by HWPSE on (11-20) Al_2O_3 substrates using a high-temperature-annealed ZnO self-buffer layer (HITAB).

As planned, we fabricated and settled a new HWPSE equipment, which has a multiple-target holder that can hold 4 different targets enabling the growth of layered structures without exposing interfaces in air. Also, since it has a load-lock system, we succeeded to improve epilayer qualities. The ZnO epilayers grown on (11-20) Al_2O_3 substrates had very smooth surface with 0.26-nm-thick atomic layer steps. Also, pole figure of the {10-11} ZnO peaks exhibited perfect six-fold symmetry peaks without any amorphous-like residues. By using HITAB on (11-20) Al_2O_3 substrates, which exhibited very narrow FWHM for the (0002) x-ray rocking curve as small as 25 arcsec, we eventually observed excitonic polariton emissions originating from free A- and B-excitons at 9 K. Single-phase MgZnO alloys were also successfully grown by HWPSE method. These achievements enable to fabricate MgZnO/ZnO heterostructures by HWPSE.

(2) Determination of exact energies of longitudinal and transverse excitons in polar (0001) and nonpolar (11-20) ZnO epilayers

Using (0001) and (11-20) ZnO epilayers grown by laser-assisted MBE method, we determined exact energies of excitonic polaritons. Polarized optical reflectance (OR), photoreflectance (PR), and photoluminescence (PL) spectra of the bulk and epitaxial ZnO were recorded at 8 K. Energies of PR resonances corresponded to those of upper and lower exciton-polariton branches, where A-, B-, and C-excitons couple simultaneously to an electromagnetic wave. PL peaks due to the corresponding polariton branches were observed. Longitudinal-transverse splittings (ω_{LT}) of the corresponding excitons were 1.5, 11.1, and 13.1 meV, respectively. The latter two values are more than two orders of magnitude greater than that of GaAs being 0.08 meV. Also, polarized OR and PR spectra of an out-plane nonpolar $(11\bar{2}0)$ ZnO epilayer grown by laser-assisted molecular beam epitaxy (L-MBE) were measured, since ZnO quantum wells (QWs) grown in nonpolar orientations are expected to show higher emission efficiencies due to the elimination of both spontaneous and piezoelectric polarization fields normal to the QW plane. They exhibited in-plane anisotropic exciton resonances according to the polarization selection

rules for anisotropically-strained wurzite material.

(3) Characterization of ZnO epilayers by time-resolved photoluminescence (TRPL) and monoenergetic positron annihilation methods, and elimination of point defects as a fundamental pathway in improving quantum efficiency of excitonic emissions in ZnO epilayers grown by L-MBE

Impacts of point defects on the nonradiative processes in L-MBE ZnO were studied using time-resolved PL making a connection with the results of positron annihilation measurement. Free excitonic PL intensity at room temperature naturally increased with the increase in nonradiative lifetime (τ_{nr}). The value of τ_{nr} increased and density or size of Zn vacancies (V_{Zn}) decreased with increasing growth temperature (T_g) in heteroepitaxial films grown on a $ScAlMgO_4$ substrate, and the use of homoepitaxial substrates further reduced V_{Zn} density. The value of τ_{nr} was shown to increase with the decrease in gross density of neutral and positively- and negatively-charged point defects including complexes rather than with the decrease in V_{Zn} density. The results indicate that nonradiative recombination process is governed not by single point defects, but by certain defects introduced with the incorporation of V_{Zn}, such as V_{Zn}-defect complexes. As a result of point defect elimination by growing the films at high T_g followed by subsequent post-growth *in situ* annealing, combined with the use of HITAB ZnO, a record long τ_{nr} for the spontaneous emission as long as 3.8 ns was obtained at room temperature. Also, rich structures due to longitudinal-transverse splitting of exciton-polaritons and excited states of excitons were found in the low-temperature PL spectrum of the epilayer that exhibited η_{int}=6.3% at 300 K. By using progressively improving epitaxial growth methods, polariton laser effect due to Bose condensation will be observed at room temperature in the near future.

(4) Dielectric SiO_2/ZrO_2 distributed Bragg reflectors for ZnO microcavities prepared by reactive helicon-wave-excited-plasma sputtering and e-beam evaporation

To deposit SiO_2 / ZrO_2 multilayer structures for DBR application, we prepared another HWPS equipment for reactive helicon-wave-excited-plasma sputtering (R-WHPS), which has a dual-target holder. By using the machine, R-HWPS method was developed to fabricate high reflectivity (*R*) DBRs tuned at the resonance wavelength of B-excitons in ZnO (366.5 nm) employing quarter-wavelength multilayers of SiO_2 and ZrO_2 dielectric films. According to the surface-damage-free nature and better stoichiometry controllability of R-HWPS method, dense films exhibiting ideal refractive indices (1.46 for SiO_2 and 2.10 for ZrO_2 at 633 nm, being similar to the bulk values) having small root-mean-square (RMS) values for the surface roughness (0.20 nm for SiO_2 and 0.53 nm for ZrO_2) were deposited at room temperature using Si and Zr targets and O_2 gas. Optical reflectance spectra of the SiO_2/ZrO_2 DBRs agreed with those calculated using the optical multilayer film theory, and the 8-pair DBR exhibited *R* higher than 99.5% at around 366.5 nm and the stop-band width (R >95%) as broad as 82 nm. These values were indeed better than those obtained from the films / DBRs fabricated by e-beam (EB) evaporation method. The results indicate that R-HWPS is a suitable technique for the sputtering of insulating films, especially to fabricate the DBRs for the realization of polariton lasers using ZnO microcavities.

(5) Growth of AlN on GaN/sapphire templates using NH_3-MBE for DBR application

As the first step to fabricate AlGaN/AlGaN heterostructures for our DBR, AlN films were grown by NH_3-MBE. Temporal evolution of surface morphology in NH_3-MBE AlN epilayers on the MOVPE-grown GaN / (0001) Al_2O_3 epitaxial templates was correlated with changes in sign and degree of the residual strain by increasing the layer thickness. They began to crack for the

thickness as thin as 10 nm. However, atomic-layer step-and-terrace surface structures were maintained for the thickness up to 32 nm. Tensile biaxial stress decreased with further increase in the thickness due to the lattice relaxation, which caused surface roughening. An 1580-nm-thick, nearly strain-compensated AlN epilayer exhibited excitonic photoluminescence (PL) peaks at 6.002 and 6.023 eV at 9 K and a near-band-edge peak at 5.872 eV at 293 K. We will grow ALN/AlGaN or AlGaN/AlGaN DBRs in the future.

Report on **"In-situ monitoring of Zn^* and Mg^* species during HWPSE of ZnO and $Mg_{0.06}Zn_{0.94}O$ films, and observation of excitonic polariton emissions from ZnO epilayers using HITAB base layer"**

Abstract

Atomic species in the sputtered plumes from pure ZnO and ZnO-MgO (94:6 mol%) targets were identified by means of plume emission spectroscopy (PES) during helicon-wave-excited-plasma sputtering epitaxy (HWPSE). Dominant Zn and Mg species detected by PES were excited neutral zinc (Zn^*) and magnesium (Mg^*), respectively. Their densities were uniquely controlled by the target bias (V_t) that accelerates the velocity of Ar cations, keeping the gross plasma density constant. The growth rate was principally limited by the densities of Zn^* and Mg^*, as well as nonradiative species such as Zn-O and Mg-O, and the MgO molar fraction x in the $Mg_xZn_{1-x}O$ epilayers nearly agreed with that of the target between 500 and 650 °C. Structural qualities of the epilayers were significantly improved by the use of nearly lattice-matched substrates having proper surface arrangements. The *a*-axis-locked single-domain (0001) $Mg_xZn_{1-x}O$ epitaxy was accomplished on an uniaxially quasi-lattice-matched (11-20) Al_2O_3 substrate. The epilayers had atomically-smooth surfaces, and 0.26-nm-high monolayer steps were observed in ZnO epilayers. Also, the pole figure of the {10-11} ZnO peaks exhibited perfect six-fold symmetry peaks without any amorphous-like residues. The ZnO films grown at low temperature (300 °C) on (11-20) Al_2O_3 substrates and subsequently annealed at high temperature (900 °C) had very smooth surface exhibiting small FWHM value for the (0002) x-ray rocking curve as small as 25 arcsec. These layers named HITAB were used as a self-buffer for the high temperature growth of ZnO. By using HITAB, we eventually observed exciton-polariton emissions originating from transverse and longitudinal free A- and B-excitons at 9 K from ZnO epilayers grown at 750 °C. Single-phase $Mg_{0.06}Zn_{0.94}O$ alloys were also successfully grown by HWPSE method. The ZnO and $Mg_{0.06}Zn_{0.94}O$ epilayers exhibited a predominant near-band-edge photoluminescence peak at room-temperature (3.29 and 3.36 eV, respectively). These achievements encourage us to fabricate MgZnO/ZnO heterostructures by HWPSE.

Introduction

In recent years, wurzite ZnO and related alloys $Mg_xZn_{1-x}O$ and $Cd_yZn_{1-y}O$ are attracting attention as promising candidates for the use of light emitters and detectors operating in visible to ultraviolet (UV) spectral regions due to their large bandgap energy (E_g) covering from 3.3 eV for ZnO to 4.5 eV for $Mg_{0.5}Zn_{0.5}O$ [1]. To fabricate UV optoelectronics devices, formation of $ZnO/Mg_xZn_{1-x}O$ heterostructures and quantum wells having abrupt interfaces is one of the essential issues. However, the $Mg_xZn_{1-x}O$ alloy growth is still immature, since the thermodynamic solid solubility of MgO in ZnO has been reported to be smaller than 4 mol% at 1200 °C [2], primarily due to the large structural dissimilarity between wurzite ZnO and rocksalt MgO. This structural gap essentially causes a phase separation and segregation triggered by the strain, and limits the maximum MgO molar fraction x in $Mg_xZn_{1-x}O$ films up to 0.5 [1]. Moreover, structural, electrical, and optical characteristics of single phase wurzite $Mg_xZn_{1-x}O$ alloy films strongly depend on the growth conditions as well as the growth methods.

Epitaxial ZnO and $Mg_xZn_{1-x}O$ films have been grown by a variety of methods such as laser-assisted molecular beam epitaxy (L-MBE) [3-9], MBE [1,10-15], chemical vapor deposition (CVD) [16,17], and metalorganic vapor phase epitaxy (MOVPE) [18,19]. However, few reports have been published on the sputtering deposition of $Mg_xZn_{1-x}O$ alloy films [20]. Sputtering methods can prepare large-area films of well-controlled compositions economically. The growth

rate can be adjusted high enough for thick films and low enough for ultrathin films principally by changing the sputtering rate of the target. Therefore, metals of high melting temperature, transparent conducting oxides, and photovoltaic layer structures have been prepared by sputtering techniques. However, there are some essential problems such as resputtering and surface damage caused by high energy sputtering particles. In order to overcome these problems and to make use of the advantages of sputtering techniques for thin film epitaxy, the authors have proposed [21] the use of helicon-wave-excited plasma (HWP), of which physics and experiments have been reported in early 90's [22-25], as a sort of remote plasma source. As a result of the process optimization, epitaxial growth of ZnO on (0001) Al_2O_3 substrates has been realized, and the technique was named *helicon-wave-excited-plasma sputtering epitaxy* (HWPSE) [26].

In this report, results of plume emission spectroscopy (PES) on ZnO and ZnO-MgO (94:6 mol%) targets are shown to identify the atomic species responsible for the $Mg_xZn_{1-x}O$ epitaxial formation. The dominant Zn and Mg species detected by PES were excited neutral Zn (Zn^*) and Mg (Mg^*), respectively. Their densities were found to be uniquely controlled by the target bias that accelerates the Ar cation velocity. The growth rate is considered to be limited by the densities of them and nonradiative species such as Zn-O and Mg-O. The ZnO and $Mg_{0.06}Zn_{0.94}O$ epilayer qualities were significantly improved by the use of the substrates having smaller lattice-mismatch and proper surface arrangement. The structural quality of ZnO epilayers were significantly improved by the postgrowth in-situ annealing at temperatures higher than 850 °C. By using high-temperature-annealed ZnO self-buffer (HITAB), we eventually observed excitonic polariton emissions originating from transverse and longitudinal free A- and B-excitons at 9 K from ZnO epilayers grown at 750 °C. The bandgap of $Mg_{0.06}Zn_{0.94}O$ films was confirmed by optical reflectance (OR) and photoluminescence (PL) measurements to be larger than that of ZnO, indicating the formation of single-phase semiconductor alloys by the HWPSE method.

Experiment

The ZnO and $Mg_{0.06}Zn_{0.94}O$ films were grown using the HWPSE apparatus [26,27]. A 99.999 %-pure undoped ZnO or a 99.99 %-pure undoped ZnO-MgO (94:6 mol%) thermally synthesized target was placed on the target holder. The HWP excited in a quartz tube from the 99.9995 %-pure Ar / 99.99995 %-pure O_2 mixture was introduced into the chamber by the weak magnetic field gradient, and the velocity of Ar cations onto the target was accelerated by the negative dc target bias (V_t) applied on back of the holder. Our configuration [21,26,27] enabled depositing thin films softly due to the elimination of plasma bombardment of the substrate, which was located off-axis from the azimuth connecting the center of the quartz tube and the target. Details of the HWPSE system will be found elsewhere [26]. The emission from the sputtered plumes was introduced to a monochromator through a pure quartz viewport that is located between the target and the substrate. Then, it was dispersed by a grating and detected using a charge-coupled device (CCD) array.

Approximately 0.6 - 1.0-μm-thick ZnO films were grown on (0001) and (11-20) Al_2O_3 substrates and on the (0001) AlN epitaxial template grown by low-pressure MOVPE [28], which consisted of a 2-μm-thick undoped AlN on a (0001) Al_2O_3 substrate. Structural and optical properties of the AlN template will be found elsewhere [28,29]. The Al_2O_3 substrates and AlN template were cleaned by organic solvents and rinsed in a DI water. They were loaded into the chamber and baked in vacuum prior to the growth. The growth temperature (T_g) was varied from 600 to 750 °C (typically 700 °C).

Approximately 100-nm-thick ZnO films grown at low temperature (300-450 °C) on the nucleation layer, which was deposited at 200 °C and subsequently annealed at 650 °C, were subjected to subsequent post-growth annealing at 900 °C, in order to confirm if ZnO films grown

by HWPSE can be used as the high-temperature-annealed self-buffer (HITAB) [30]. Approximately 1-μm-thick ZnO epilayers were grown at 700-900 °C on these HITAB base layers.

Typical rf power (P_{rf}), V_t, background pressure, and growth pressure were 700 W, -360 V, 4×10^{-6} Torr, and 5×10^{-4} Torr, respectively. Approximately 0.6 - 0.8 μm-thick $Mg_xZn_{1-x}O$ films were grown exclusively on the (11-20) Al_2O_3 substrate, since the film qualities of ZnO on the (11-20) Al_2O_3 substrate were found during the course of this work to be superior than those of the films grown on other lattice-mismatched substrates. Somewhat lower T_g between 550 and 650 °C was used for the MgZnO growth (typically 600 °C). Other growth parameters were identical to those used for the ZnO growth. To estimate the incorporation rate of MgO in ZnO matrix as a function of T_g, the film was also deposited at 70 °C. The MgO molar fraction, x, in the $Mg_xZn_{1-x}O$ films were quantified by electron-probe micro analysis (EPMA).

The crystallographic orientations and mosaicity were characterized by x-ray diffraction (XRD) measurements with a four-axes goniometer. The surface morphology was observed by atomic-force microscopy (AFM). Near normal-incidence OR spectra were measured at 293 K using a white light from a Xe lamp. The reflected light was dispersed by a grating and detected using a CCD array. The PL was excited by the 325.0 nm line of a cw He-Cd laser (15 mW), and was dispersed by a 67-cm-focal-length grating monochromator. The signal was detected phase-sensitively by a GaAs:Cs photomultiplier.

Results and Discussion

Limiting factors of ZnO and $Mg_{0.06}Zn_{0.94}O$ growth by HWPSE

The plume emission spectra of the ZnO target sputtered under V_t= 0 and -360 V (P_{rf}=700 W) are shown in Figs. 1(a) and 1(b), respectively. The HWP consisted of excited species of oxygen atom (O^*), Ar atom (Ar^*), oxygen cation (O^{+*}), and oxygen molecule (O_2^{+*}) [31], as shown in Fig. 1(a). When the magnitude of V_t was increased to -360 V, emission lines due to excited zinc atom (Zn^*) appeared at 307 nm [32], while the intensity of O^*, Ar^*, O^{+*}, and O_2^{+*} were nearly unchanged, as shown in Fig. 1(b). Note that very weak Zn^* and Zn^{+*} signals were observed even for V_t = 0 V. This is due to the weak but finite HWP velocity toward the target, which was accelerated by the magnetic field gradient and the magnet on back of the target holder.

The intensity of Zn^* increased with increasing $|V_t|$, as shown by closed circles in Fig. 2(a). The result indicates that Zn^* is the dominant radical species in our HWPSE system, and its density can be controlled uniquely by V_t that changes the velocity of Ar cations, keeping the gross HWP density constant. This feature is different from that for the conventional sputtering methods such as dc and rf magnetron sputtering, in which the plume density is proportional to the plasma

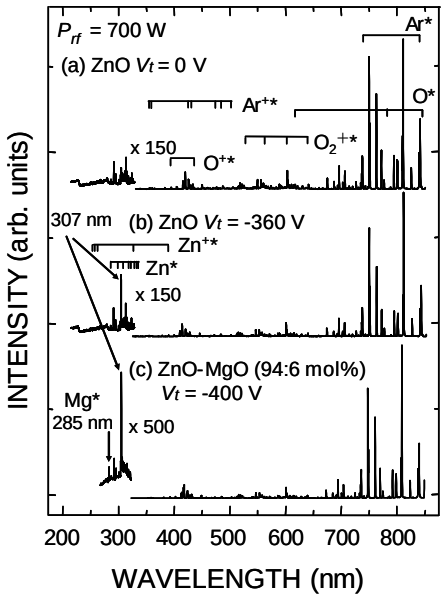

Fig. 1 Plume emission spectra of undoped ZnO target sputtered under (a) V_t = 0 V and (b) V_t = -360 V, and (c) the spectrum of undoped ZnO-MgO (94:6 mol%) target sputtered under V_t = -400 V with rf power of 700 W, where V_t is the target bias. Emission lines attributable to Zn^*, Zn^{+*}, Mg^*, O^*, O_2^{+*}, O^{+*}, Ar^*, and Ar^{+*} are indicated by respective superimposed combs (after Ref. [31]). The lines at 307 and 285 nm are due to Zn^* and Mg^*, respectively.

density. Although the density of nonradiative species such as Zn-O may also increase with $|V_t|$ and they may contribute to the film growth, the growth of ZnO by HWPSE is considered to be mainly limited by the incorporation of O from the gas phase, because the growth rate was extremely low or even zero if O was not added in the Ar plasma. The growth rate was proportional to the Zn^* density, as shown by open characters in Fig. 2(a). This feature is similar to that of L-MBE. The growth rate decreased with the increase in T_g and the film growth seems to have a threshold V_t (around -150 V at 600 °C), as shown in Fig. 2(a). These results indicate that the film growth rate is limited by the competition of Zn^* flux and reevaporation rate of ZnO due to the oxygen deficiency.

The plume emission spectra of the ZnO-MgO (94:6 mol%) target under V_t = -400 V is shown in Fig. 1(c). In addition to the Zn^* line, the emission line due to the excited Mg atom (Mg^*) appeared at 285 nm [32]. Their intensities simultaneously increased with the increase in $|V_t|$. Therefore, Mg^* is considered to contribute to the $Mg_xZn_{1-x}O$ growth. The MgO molar fraction x, in the grown films are plotted as a function of $1/T_g$ in Fig. 2(b). The value of x was close to that of the target; it increased slightly with increasing T_g with the activation energy of 0.11 kcal/mol. This slight increase may be due to faster decrease of the sticking coefficient of Zn precursor relative to that of Mg one with increasing T_g, due to the difference in their vapor pressures; it has been reported [7] that vapor pressures of Zn species were higher than those of Mg, and consequently Zn might preferentially desorb from the growing surface leaving the MgO-rich solid phase. Accordingly, in HWPSE, x in the epilayer can be controlled by $|V_t|$ and T_g, in addition to the target composition. The value of x at 600 °C could accidentally be identical to that of the target. Therefore further investigation of x as functions of O_2 partial pressure and T_g is necessary to disclose the limiting factors that control the solid composition in HWPSE of semiconductor alloys.

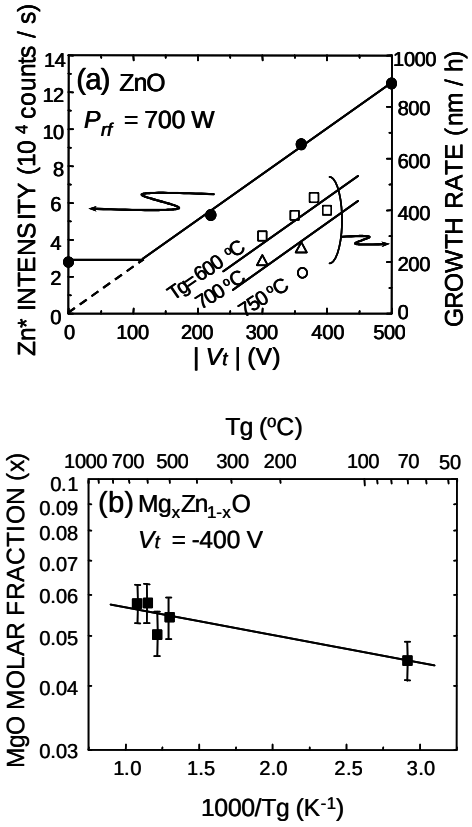

Fig. 2 (a)Emission intensity of Zn^* at 307 nm (closed circles) and ZnO growth rate (open characters) as a function of magnitude of the target bias $|V_t|$. The growth temperature was varied between 600 and 750 °C. (b) MgO molar fraction x in $Mg_xZn_{1-x}O$ films as a function of inverse growth temperature ($1/T_g$) under V_t = -400 V.

Epitaxial orientations and surface morphologies

Representative θ-2θ XRD patterns of the ZnO epilayers grown at 700 °C on (11-20) and (0001) Al_2O_3 substrates and on the (0001) AlN template [ZnO/(11-20) Al_2O_3, ZnO/(0001) Al_2O_3, and ZnO/(0001) AlN/Al_2O_3, respectively] are shown in Fig. 3(a). All the ZnO films showed (0001) orientation growth, and the values of full-width at half-maximum (FWHM) of the (0002) ZnO diffraction peak (Δ2θ), which reflect the distribution of out-plane lattice constants, were 0.13° for ZnO/(11-20) Al_2O_3, 0.18° for ZnO/(0001) AlN, and 0.19° for ZnO/(0001) Al_2O_3. They seem to increase with the increase in in-plane effective lattice mismatch; the mismatches are

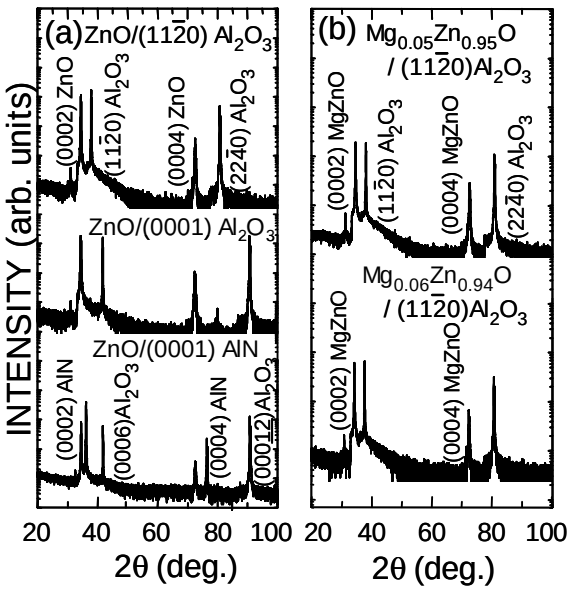

Fig. 3 XRD θ-2θ scan profiles for (a) ZnO/(11-20) Al_2O_3, ZnO/(0001) Al_2O_3, and ZnO/(0001) AlN/(0001) Al_2O_3. (b) Those for $Mg_{0.05}Zn_{0.95}O$/(11-20) Al_2O_3 and $Mg_{0.06}Zn_{0.94}O$/(11-20)Al_2O_3.

+0.08 and +2.55 %, respectively, along [11-20] and [1-100] ZnO directions for ZnO/(11-20) Al_2O_3, +4.4 % for ZnO/(0001) AlN, and +18.3 % for ZnO/(0001) Al_2O_3. Therefore, the increase in Δ2θ can be explained by the enhanced inhomogeneous lattice relaxation in highly lattice-mismatched systems. However, FWHM values of the (0002) ZnO ω-scans (Δω), which mainly reflect the crystalline mosaicity in *c*-axis, were 0.48° for ZnO/(11-20) Al_2O_3, 1.10° for ZnO/(0001) AlN, and 0.66° for ZnO/(0001) Al_2O_3.

The in-plane epitaxial relations of the ZnO epilayers grown on the (11-20) and (0001) Al_2O_3 substrates were confirmed by ϕ-scanning XRD measurements (data not shown) [33] to be [11-20] ZnO // [0001] Al_2O_3 and [1-100] ZnO // [0-110] Al_2O_3 for (0001) ZnO/(11-20) Al_2O_3 and [11-20] ZnO // [10-10] Al_2O_3 for (0001) ZnO/(0001) Al_2O_3. These relationships are the expected ones giving the smallest lattice-mismatches between the epilayers and the substrates. Figure 4 represents the XRD pole figure measured for {10-11} reflection of the ZnO epilayers grown on (11-20) Al_2O_3. Negligible amorphous-like residue was found for the film grown by the new system, indicating that the use of load-lock and purification of the system improved the interface qualities. Conversely, the ZnO/(0001) AlN film showed a multidomain growth whose *a*-axes were parallel to either ⟨11-20⟩ or ⟨10-10⟩ AlN. One of the reasons for the multi-domain growth is attributed to the small difference in the effective lattice-mismatches between the epitaxial relations [11-20] ZnO // [11-20] AlN (+4.4 %) and [11-20] ZnO // [10-10] AlN (-9.7 %). Another reason for the multidomain growth and the large *c*-axis mosaicity may be the presence of Al-suboxynitrides at the ZnO/AlN interface due to the natural oxidation of the AlN surface, since the pregrowth surface treatment of AlN is in principle difficult and the overlayer (ZnO) contains O in the matrix. Formation of polycrystalline spinel $ZnAl_2O_4$, whose *a*-axis length is 0.80848 nm, at the ZnO/AlN interface [34] is also probable. Moreover, formation of inversion domains must be considered, since most of III-nitride epilayers grown by MOVPE grow toward the (0001) face (group-III polarity) [35,36] while ZnO epilayers grown by L-MBE usually grow toward the (000-1) face (O-polarity) [37]. Therefore, proper deoxidation and purification

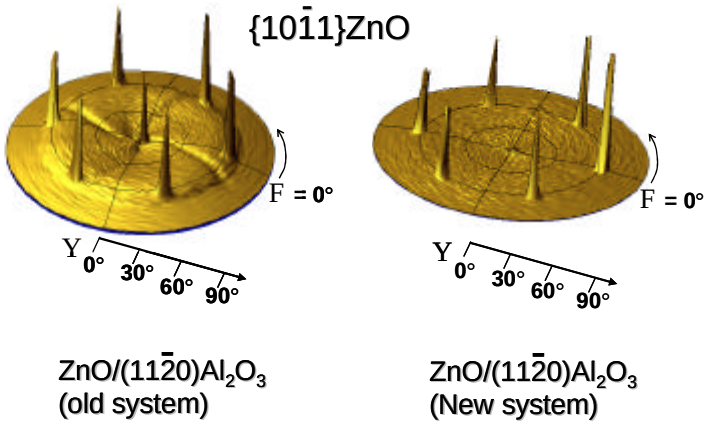

Fig.4 XRD pole figure measured using {10-11} reflection for the ZnO epilayers grown on (11-20) Al_2O_3 substrates by HWPSE. Negligible amorphous-like residue was found for the film grown by the new system.

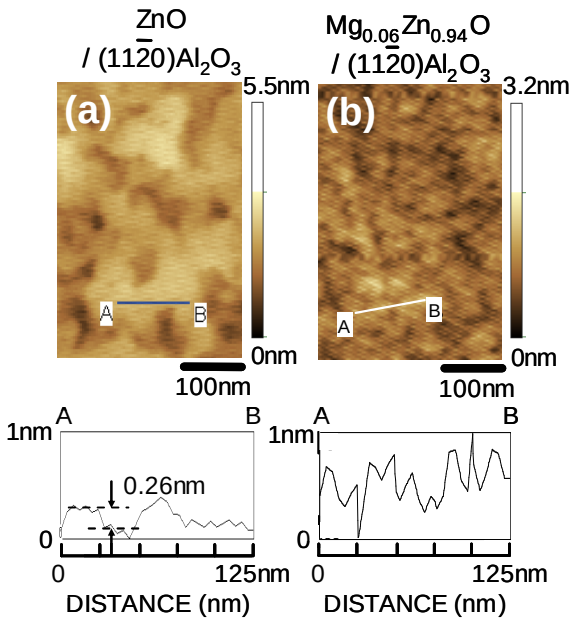

Fig. 5 AFM images of (a) ZnO and (b) $Mg_{0.06}Zn_{0.94}O$ epilayers grown on (11-20) Al_2O_3 substrates. Cross-sectional height profiles are also shown in the bottom panels. The step height 0.26 nm corresponds to a half of the *c*-lattice parameter of ZnO.

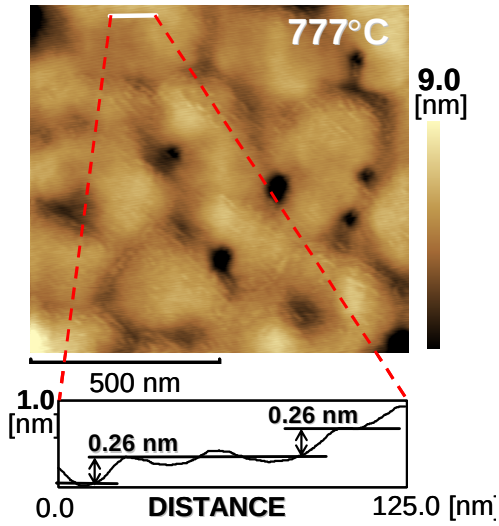

Fig. 6 AFM image of ZnO epilayers grown by HWPSE at 777 °C.

techniques for the AlN surface, as well as the insertion of an appropriate buffer layer are necessary for a single-domain ZnO/AlN heteroepitaxy.

The θ-2θ XRD patterns of $Mg_{0.05}Zn_{0.95}O$ and $Mg_{0.06}Zn_{0.94}O$ epilayers grown on the in-plane uniaxially nearly lattice-matched (11-20) Al_2O_3 substrates are shown in Fig. 3(b). Both of the films showed the (0001) orientation growth, and no extra phase was detected. Also, the in-plane epitaxial relations [11-20] MgZnO // [0001] Al_2O_3 and [1-100] MgZnO // [0-110] Al_2O_3 were confirmed from the results of ϕ-scanning XRD measurement. Values of Δ2θ and Δω of the (0002) $Mg_xZn_{1-x}O$ diffraction were 0.17 and 0.60~0.65°, respectively. They are larger than those of ZnO films on the (11-20) Al_2O_3 substrates, indicating the enhanced compositional fluctuation, strain fluctuation, and tilting.

The ZnO epilayer grown on the (11-20) Al_2O_3 substrate at 700 °C had a smooth surface with atomically flat, approximately 50-100-nm-wide two-dimensional (2D) terraces, as shown in the AFM image in Fig. 5(a). The step height at the edge of the 2D islands was 0.26 nm, which corresponds to a half of the *c*-axis length. Figure 6 also shows the surface morphology of the ZnO epilayer grown using a new system, which showed atomic layer staircases. On the other hand, clear step-and-terrace feature was not observed for the $Mg_{0.06}Zn_{0.94}O$ film, as shown in Fig. 5(b), though the root-mean-square (RMS) roughness of the film was as small as 0.38 nm. The reason for the irregular surface structure may be the shorter terrace width due to the insufficient surface diffusion length, since T_g was lowered compared to the ZnO growth in order to improve the RMS roughness value.

Optical properties

OR and PL spectra of ZnO/(11-20) Al_2O_3 and $Mg_xZn_{1-x}O$/(11-20) Al_2O_3 (x = 0.05 and 0.06) films measured at 293 K are shown in Fig. 7. The OR spectra exhibited clear interference fringes, which are due to the multiple internal reflection between the surface and epilayer / substrate interface. Usually, OR spectrum of a direct bandgap semiconductor thin film exhibits excitonic

reflectance anomalies slightly above the photon energy at which the multiple interference fringes vanish. However, such structures could not be seen in Fig. 7. Therefore, effective excitonic bandgap E_{ex} was defined as the energy at which the fringes vanish. This method seems to be reliable, since E_{ex} of the ZnO film determined in this way (3.30 eV for x= in Fig. 7) nearly agreed with the A-excitonic resonance energy (3.305 eV [38]) of the ZnO epilayer grown by the L-MBE method at room temperature. The energy position of E_{ex} are marked by the arrows in Fig. 7. The E_{ex} values obtained for the $Mg_xZn_{1-x}O$ epilayers (3.45-3.48 eV for x=0.05-0.06) are larger than that of ZnO, and the values are comparable to that reported for the $Mg_{0.05}Zn_{0.95}O$ epilayer grown by L-MBE (≅3.45 eV) [7]. The result confirms the formation of a single-phase MgZnO semiconductor alloys using HWPSE method.

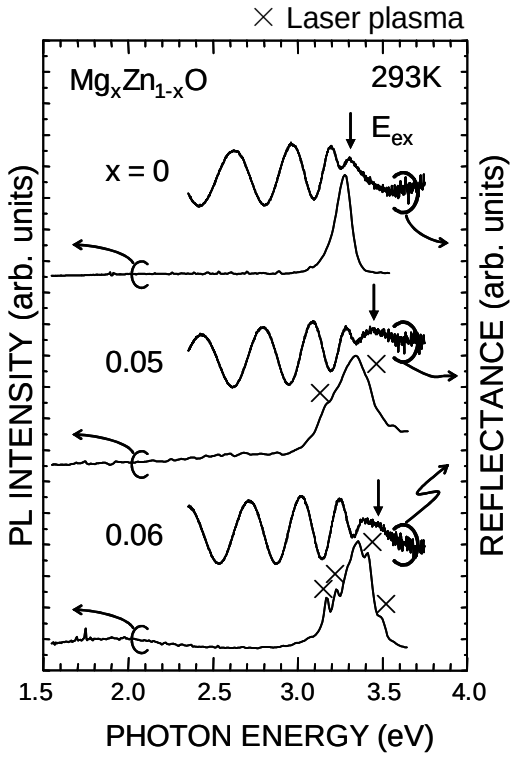

Fig. 7 PL and OR spectra of $Mg_xZn_{1-x}O$ (x = 0, 0.05, and 0.06) films measured at 293 K. The downward arrows indicate the positions of the effective excitonic bandgap, E_{ex}.

The PL spectrum of the ZnO film exhibited a predominant near-band-edge PL peak at 3.28 eV, as shown in Fig. 7. Since the energy is slightly lower than E_{ex} determined from the OR spectrum, the PL peak is assigned as being due to the recombination of excitons bound to certain impurities or defects. The FWHM value was 101 meV, which is comparable to that of the films grown by L-MBE [38] or MBE [39]. PL spectra of the $Mg_{0.05}Zn_{0.95}O$ and $Mg_{0.06}Zn_{0.94}O$ films also exhibited predominant near-band-edge peaks at 3.34 and 3.36 eV, respectively. The FWHM values were as large as 190-330 meV, which cannot be explained by the classical alloy broadening model [40]. Also, the energy differences between E_{ex} and the PL peaks (Stokes-type shifts) were as large as 110-120 meV. These results indicate the formation of band-tail states due mainly to the compositional inhomogeneity, as suggested from the XRD results. Further optimization of the overall growth process is needed to obtain higher quality $Mg_{0.06}Zn_{0.94}O$ epilayers.

Exciton-polariton emissions from HWPSE ZnO on high-temperature-annealed ZnO self-buffer (HITAB)

To further improve structural and optical quality of ZnO and MgZnO epilayers, the use of high-temperature-annealed ZnO self-buffer (HITAB) [30] is considered to be very effective, as is the case with L-MBE of ZnO on SCAM substrate, which is described in the next section of this report. The concept of HITAB is to obtain strain-free and structurally coherent ZnO epitaxial base on a nearly lattice-matched substrate for the overlayer epitaxial growth using surface mass-transport, by annealing thin ZnO layer grown at low temperature at temperatures higher than the overlayer growth temperature [30]. In this work, a 100-nm-thick ZnO layer grown at 300 °C on a crystallized nucleation layer deposited at 200 °C on a (11-20) Al_2O_3 substrate, was annealed at 900 °C for 1 h in O_2 ambient (10^{-4} Torr). Subsequently, ZnO epitaxial overlayer was grown at 750 °C. The AFM image of HITAB base layer prepared in this way is shown in Fig. 8. Although the surface RMS roughness was approximately 0.2 nm, grain boundaries seen in Figs. 5 and 6

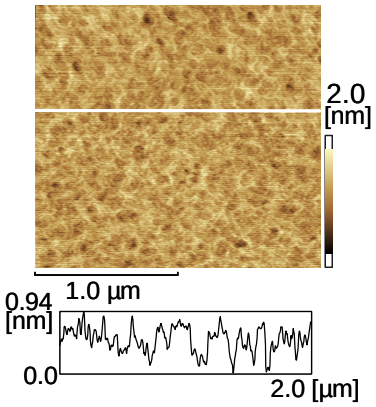

Fig. 8 AFM image and height profile of ZnO HITAB.

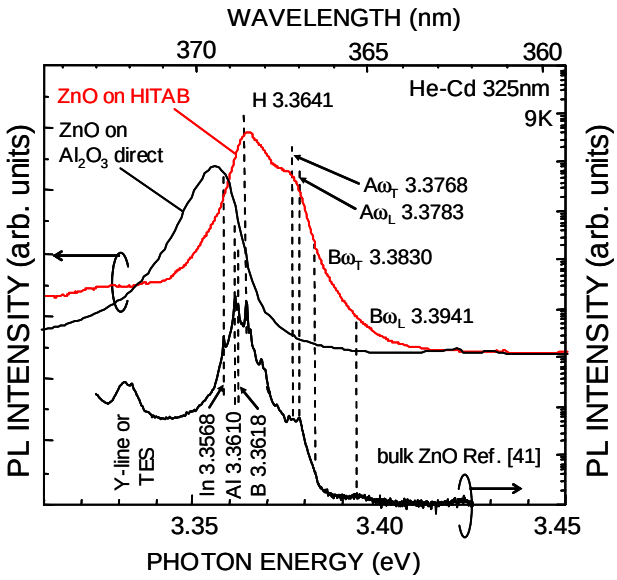

Fig. 9 PL specta at 9 K of 1-µm-thick ZnO epilayers grown by HWPSE at 750 °C. Red curve is for the one grown on HITAB base layer and black curve is for the one grown directly on (11-20) Al_2O_3. PL spectrum of the bulk ZnO crystal [41] is also shown for comparison.

due to the small lattice mismatch between ZnO and *a*-axis of Al_2O_3 (+0.08 %) are no longer seen in wide-area, and FWHM of (0002) XRC peak was greatly reduced to 25 arcsec, which is similar to that obtained for L-MBE HITAB grown on SCAM substrate.

PL spectra at 9 K of approximately 1-µm-thick ZnO epilayer grown at 750 °C on the HITAB base (red curve) and that grown directly on (11-20) Al_2O_3 are shown in Fig. 9. In Fig. 9, PL spectrum of the bulk ZnO (Eagle Picher) [41] is also shown in logarithmic vertical scale for comparison. Different from the PL spectrum of the ZnO film grown directly on Al_2O_3, pronounced free A exciton peak around 3.378 eV and shoulders originating from longitudinal and transverse B excitons ($B\omega_L$ and $B\omega_T$, respectively) are found in the PL spectrum of ZnO on HITAB, although the spectral lineshape is broadened due presumably to the lattice strain inhomogeneity. The results indicate that HWPSE can grow good quality ZnO film for cavity-coupled polariton laser application, when appropriate base layer is prepared, for example, HITAB ZnO in this study.

Conclusions

Atomic species responsible for the $Mg_xZn_{1-x}O$ formation in HWPSE were identified to be Zn^* and Mg^*, as well as nonradiative species such as Zn-O and Mg-O, by means of plume emission spectroscopy. The Zn^* and Mg^* emission intensities could be controlled by the magnitude of V_t, which accelerates the velocity of Ar cations onto the target, independently to the gross HWP density. The growth rate was essentially limited by the densities of active Zn^* and Mg^*. The MgO molar fraction in the $Mg_xZn_{1-x}O$ epilayers grown between 550 and 600 °C nearly agreed with that of the target being 0.06. The importance of both lattice-matching and preparation of proper surface arrangement of the substrate was shown, and the use of in-plane uniaxially quasi-lattice-matched (11-20) Al_2O_3 substrates enabled to fabricate *a*-axis-locked, single-domain epilayers having atomically smooth 2D terraces with monolayer steps. Approximately 100-nm-thick ZnO layers grown at low temperature (300-450 °C) on the nucleation layer, which was deposited at 200 °C and subsequently annealed at 650 °C, were subjected to subsequent post-growth annealing at 900 °C. These layers named HITAB had very smooth surface exhibiting small FWHM value for (0002) x-ray rocking curve as small as 25

arcsec, and were used as a self-buffer for the high temperature growth of ZnO. By using HITAB, we eventually observed exciton-polariton emissions originating from transverse and longitudinal free A- and B-excitons at 9 K from ZnO epilayers grown at 750 °C. The effective bandgap and PL peak energy shifted to the higher energy as the MgO molar fraction increased. HWPSE method can be regarded as one of the promising epitaxial fabrication techniques to form high-quality quantum heterostructures having atomically abrupt heterointerfaces for future device applications.

Acknowledgments

We than Dr. M. Tanaka and Dr. T. Shibata of NGK Insulators Inc. for supplying the AlN/Al_2O_3 epitaxial template.

References

[1] T. Takagi, H. Tanaka, Sz. Fujita, and Sg. Fujita, Jpn. J. Appl. Phys., Part 2 **42**, L401 (2003).
[2] J. F. Sarver, F. L. Katnack, and F. A. Hummel, J. Electrochem. Soc. **106**, 960 (1959).
[3] P. Yu, Z. Tang, G. Wong, M. Kawasaki, A. Ohtomo, H. Koinuma, and Y. Segawa, *Proc. 23rd Int'l Conf. on Physics of Semicond.*, Berlin, eds. M. Scheffler and R. Zimmermann (World Scientific, Singapore, 1996), vol. 2, p. 1453; Solid State Commun. **103**, 459 (1997).
[4] A. Ohtomo, M. Kawasaki, Y. Sakurai, Y. Yoshida, H. Koinuma, P. Yu, Z. Tang, G. Wong, and Y. Segawa, Mater. Sci. Eng. B **54**, 24 (1998).
[5] S. Choopun, R. Vispute, W. Noch, A. Balsamo, R. Sharma, T. Venkatesan, A. Iiadis, and D. C. Look, Appl. Phys. Lett. **75**, 3947 (1999).
[6] M. Joseph, H. Tabata, and T. Kawai, Jpn. J. Appl. Phys. Part 2 **38**, L1205 (1999); M. Joseph, H. Tabata, H. Saeki, K. Ueda, and T. Kawai, Physica B **302-303**, 140 (2001).
[7] A. Ohtomo, M. Kawasaki, T. Koida, K. Masubuchi, H. Koinuma, Y. Sakurai, Y. Yoshida, T. Yasuda, and Y. Segawa, Appl. Phys. Lett. **72**, 2466 (1998).
[8] A. K. Sharma, J. Narayan, J. F. Muth, C. W. Teng, C. Jin, A. Kvit, R. M. Kolbas, and O. W. Holland, Appl. Phys. Lett. **75**, 3327 (1999).
[9] S. Choopun, R. D. Vispute, W. Yang, R. P. Sharma, and T. Venkatesan, Appl. Phys. Lett. **80**, 1529 (2002).
[10] J. Cook and F. Schetzina, J. Electron. Mater. **25**, 855 (1996).
[11] D. Bagnall, Y. Chen, Z. Zhu, T. Yao, S. Koyama, M. Shen, and T. Goto, Appl. Phys. Lett. **70**, 2230 (1997); *ibid* **73**, 1038 (1998).
[12] K. Iwata, P. Fons, A. Yamada, K. Matsubara, and S. Niki, J. Cryst. Growth **209**, 526 (2000); P. Fons, K. Iwata, S. Niki, A. Yamada, K. Matsubara, and M. Watanabe, *ibid* **209**, 532 (2000).
[13] P. Fons, K. Iwata, A. Yamada, K. Matsubara, S. Niki, K. Nakaha, T. Tanabe, and H. Takasu, Appl. Phys. Lett. **77**, 1801 (2000); J. Cryst. Growth **227/228**, 911 (2001).
[14] K. Nakahara, H. Takasu, P. Fons, K. Iwata, A. Yamada, K. Matsubara, R. Hunger, and S. Niki, J. Cryst. Growth **227/228**, 923 (2001).
[15] K. Ogata, K. Koike, T. Tanite, T. Komuro, F. Yan, S. Sasa, M. Inoue, and M. Yano, J. Cryst. Growth **251**, 623 (2003).
[16] K. Minegishi, Y. Koiwai, Y. Kikuchi, K. Yano, M. Kasuga, and A. Shimizu, Jpn. J. Appl. Phys., Part 2 **36**, L1453 (1997).
[17] S. Muthukumar, J. Zhong, Y, Chen, and Y. Lu, Appl. Phys. Lett. **82**, 742 (2003).
[18] K. Ogata, T. Kawanishi, K. Maejima, K. Sakurai, S. Fujita, and Sg. Fujita, Jpn. J. Appl. Phys., Part 2 **40**, L657 (2001).

[19] W. I. Park, G. C. Yi, and H. M. Jang, Appl. Phys. Lett. **79**, 2022 (2001).
[20] T. Minemoto, T. Negami, S. Nishiwaki, H. Takakura, and Y. Hamakawa, Thin Solid Films **372**, 173 (2000).
[21] K. Yamaya, Y. Yamaki, H. Nakanishi, and S. Chichibu, Appl. Phys. Lett. **72**, 235 (1998).
[22] F. Chen, Plasma Phys. and Controlled Fusion, **33**, 339 (1991); J. Vac. Sci. Technol. A **10**, 1389 (1992).
[23] R. Boswell, *Proc. of 21st Int'l Conf. on Phenomena in Ionised Gases*, eds. G. Ecker, U. Arendt, J. Boseler, and A. Brunn (Arbeitsgemeinschaft Plasma Physik, Bochum, 1993), pp.18.
[24] T. Nakano, K. Giapis, R. Gottscho, T. Lee, and N. Sadeghi, J. Vac. Sci. Technol. B **11**, 2046 (1993).
[25] H. Sugai, Oyo Buturi **63**, 559 (1994) [in Japanese].
[26] S. F. Chichibu, T. Yoshida, T. Onuma, and H. Nakanishi, J. Appl. Phys. **91**, 874 (2002).
[27] T. Koyama, T. Onuma, and S. F. Chichibu, Appl. Phys. Lett. **83**, 2973 (2003).
[28] T. Shibata, K. Asai, Y. Nakamura, M. Tanaka, K. Kaigawa, J. Shibata, and H. Sakai, J. Cryst. Growth **229**, 63 (2001); T. Shibata, Y. Kida, H. Miyake, K. Hiramatsu, K. Asai, T. Nagai, S. Sumiya, M. Tanaka, and O. Oda, *Proceedings of the 28th International Symposium on Compound Semiconductors*, University of Tokyo, Japan, 1-4 Oct. 2001, TuP-30.
[29] T. Onuma, S. F. Chichibu, T. Sota, K. Asai, S. Sumiya, T. Shibata, and M. Tanaka, Appl. Phys. Lett. **81**, 652 (2002).
[30] A. Tsukazaki, A. Ohtomo, S. Yoshida, M. Kawasaki, C. H. Chia, T. Makino, Y. Segawa, T. Koida, S. F. Chichibu, and H. Koinuma, Appl. Phys. Lett. **83**, 2784 (2003).
[31] C. E. Moore, *Atomic energy leves*, (Government Printing Office Washington, D. C., 1949); G. Herzberg, *Molecular spectra and Molecular structure*, (Van Nostrand, New York, 1967).
[32] F. Claeyssens, A. Cheesman, S. J. Henley, and M. N. R. Ashfold, J. Appl. Phys. **92**, 6886 (2002); Y. Chen, D. M. Bagnall, H. Koh, K. Park, K. Hiraga, Z. Zhu, and T. Yao, *ibid* **84**, 3912 (1998).
[33] T. Koyama and S. F. Chichibu, J. Appl. Phys. **95**, 7856 (2004).
[34] J. Narayan, K. Dovidenko, A. K. Sharma, and S. Oktyabrsky, J. Appl. Phys. **84**, 2597 (1998).
[35] M. Sumiya, M. Tanaka, K. Ohtsuka, S. Fuke, T. Ohnishi, I. Ohkubo, M. Yoshimoto, H. Koinuma, and M. Kawasaki, Appl. Phys. Lett. **75**, 674 (1999).
[36] M. Sumiya, K. Yoshimura, T. Ito, K. Ohtsuka, S. Fuke, K. Mizuno, M. Yoshimoto, H. Koinuma, A. Ohtomo, and M. Kawasaki, J. Appl. Phys. **88**, 1158 (2000).
[37] T. Ohnishi, A. Ohtomo, M. Kawasaki, K. Takahashi, M. Yoshimoto, and H. Koinuma, Appl. Phys. Lett. **72**, 824 (1998).
[38] S. F. Chichibu, A. Tsukazaki, M. Kawasaki, K. Tamura, Y. Segawa, T. Sota, and H. Koinuma, Appl. Phys. Lett. **80**, 2860 (2002).
[39] S. F. Chichibu, T. Sota, P. J. Fons, K. Iwata, A. Yamada, K. Matsubara, and S. Niki, Jpn. J. Appl. Phys. **41**, L935 (2002).
[40] E. F. Schubert, E. O. Goebel, Y. Horikoshi, K. Ploog, and H. J. Queisser, Phys. Rev. B **30**, 813 (1984).
[41] S. F. Chichibu, T. Sota, G. Cantwell, D. B. Eason, and C. W. Litton, J. Appl. Phys. **93**, 756 (2003).

Report on **"Toward the realization of cavity polariton lasers; Determination of exciton-polariton energies, relation between the nonradiative lifetime and point defect density, and elimination of point defects as a fundamental pathway in improving quantum efficiency of excitonic emissions in ZnO epilayers grown by L-MBE"**

Abstract

Static and dynamic responses of excitons in state-of-the-art bulk and epitaxial ZnO were investigated to support the possible realization of polariton lasers, which are coherent and monochromatic light sources due to Bose condensation of exciton-polaritons in semiconductor microcavities (MCs). To grasp the current problems and to pave the way for obtaining ZnO epilayers of improved qualities, following four principal subjects are treated: (i) Polarized optical reflectance (OR), photoreflectance (PR), and photoluminescence (PL) spectra of the bulk and epitaxial ZnO were recorded at 8 K. Energies of PR resonances corresponded to those of upper and lower exciton-polariton branches, where A-, B-, and C-excitons couple simultaneously to an electromagnetic wave. PL peaks due to the corresponding polariton branches were observed. Longitudinal-transverse splittings (ω_{LT}) of the corresponding excitons were 1.5, 11.1, and 13.1 meV, respectively. The latter two values are more than two orders of magnitude greater than that of GaAs being 0.08 meV. (ii) Using these values and material parameters, corresponding vacuum-field Rabi splitting of exciton-polaritons coupled to a model MC mode was calculated to be 191 meV, which is a record high value ever reported for semiconductor MCs and satisfies the requirements to observe strong exciton-light coupling regime necessary for polariton lasing above room temperature. (iii) Polarized OR and PR spectra of an out-plane nonpolar $(11\bar{2}0)$ ZnO epilayer grown by laser-assisted molecular beam epitaxy (L-MBE) were measured, since ZnO quantum wells (QWs) grown in nonpolar orientations are expected to show higher emission efficiencies due to the elimination of both spontaneous and piezoelectric polarization fields normal to the QW plane. They exhibited in-plane anisotropic exciton resonances according to the polarization selection rules for anisotropically-strained wurzite material. (iv) Impacts of point defects on the nonradiative processes in L-MBE ZnO were studied using time-resolved PL making a connection with the results of positron annihilation measurement. Free excitonic PL intensity at room temperature naturally increased with the increase in nonradiative lifetime (τ_{nr}). The value of τ_{nr} increased and density or size of Zn vacancies (V_{Zn}) decreased with increasing growth temperature (T_g) in heteroepitaxial films grown on a $ScAlMgO_4$ substrate, and the use of homoepitaxial substrates further reduced V_{Zn} density. The value of τ_{nr} was shown to increase with the decrease in gross concentration of neutral and positively- and negatively-charged point defects including complexes rather than with the decrease in V_{Zn} density. The results indicate that nonradiative recombination process is governed not by single point defects, but by certain defects introduced with the incorporation of V_{Zn}, such as V_{Zn}-defect complexes. As a result of defect elimination by growing the films at high T_g followed by subsequent post-growth *in situ* annealing, combined with the use of high-temperature-annealed ZnO self-buffer (HITAB) layer, a record long τ_{nr} for the spontaneous emission as long as 3.8 ns was obtained at room temperature. Also, rich structures due to longitudinal-transverse splitting of exciton-polaritons and excited states of excitons were found in the low-temperature PL spectrum of the epilayer that exhibited η_{int}=6.3% at 300 K. By using progressively improving epitaxial growth methods, polariton laser effect is expected to be observed at room temperature in a near future.

Introduction

ZnO and related alloys are attracting attention, since they are excellent candidates for use in visible and ultraviolet (UV) light emitters, transparent field-effect transistors, sensors, and piezoelectric devices as well as transparent conducting oxides: ZnO has a large exciton binding energy (59 meV) [1] and a large bandgap (3.4 eV) comparable to that of GaN. Rich excitonic features in ZnO have been investigated over 40 years; In 1960 Thomas [2] and Hopfield [3] assigned the sequence of three separate *p*-like valence bands in the order, Γ_{7v}^{u}, Γ_{9v} and Γ_{7v}^{l} with increasing transition energy to the *s*-like Γ_{7c} conduction band. Excitons related to the respective valence bands are referred to as A-, B- and C-excitons, respectively. On the contrary, Reynolds *et al*. [4] have assigned the ordering as A-Γ_{9v}, B-Γ_{7v}^{u} and C-Γ_{7v}^{l} by means of polarized optical reflectance (OR) and magnetoluminescence measurements. Gil [5] has supported the latter assignment by calculating the oscillator strengths of the respective excitons taking the short-range electron-hole exchange interaction into account: the band assignment is still in debate. Nevertheless, both models predict that A- and B-transitions are allowed for the light polarization *E* perpendicular to the optic (*c*-) axis ($E \perp c$), where *E* is the electric field component, and C-transition is essentially allowed for the light polarization *E* parallel to the *c*-axis ($E // c$). The resonance energies of the ground-state A-, B- and C-excitons in strain-free bulk crystals have been determined by means of OR measurements [2,4,6] to be approximately E_A=3.377, E_B=3.386 and E_C=3.4215 eV at 4.2 K.

Since excitons in ZnO are stable at room temperature [1], ZnO is of considerable interest for realization of cavity-coupled polariton lasers [7] operated at room temperature [8], in which the coherent light amplification is induced due to Bose condensation of exciton-polaritons [9], the operation principles being different from usual semiconductor lasers based on the population inversion of electron-hole plasma. Bulk and surface exciton-polaritons in ZnO single crystals, where A-, B- and C excitons couple simultaneously to an electromagnetic wave, have been investigated by Hümmer and Gebhardt [10] and Lagois [11] using angular-resolved OR and attenuated total reflection method. They have fitted the spectra theoretically taking the *exciton dead layer* into account to determine the energies of respective upper and lower polariton branches (UPB and LPB, respectively). They have obtained the longitudinal-transverse splitting (ω_{LT}), which is the energy difference between the longitudinal and transverse excitons (ω_L and ω_T, respectively), of B-exciton to be 11 meV, which was more than two orders of magnitude greater than that of GaAs being 0.08 meV. Since ω_{LT} is proportional to the oscillator strength of excitons and represents the stability of exciton-polaritons, the value predicts gigantic vacuum-field Rabi splitting (Ω_{Rabi}) of ZnO microcavity (MC) polaritons [8].

To fabricate light-emitting diodes (LEDs), laser diodes (LDs) and polariton lasers having ultrathin quantum structures of abrupt interfaces, researches on the epitaxial formation of ZnO have been accelerated using a variety of methods such as laser-assisted molecular beam epitaxy (L-MBE) [12-16], molecular beam epitaxy (MBE) [17-20], chemical vapor deposition [21], metal organic vapor phase epitaxy [22], and helicon-wave-excited plasma sputtering epitaxy [23]. As a result of the research progress, clear indication that excitonic effect is obvious even at temperatures higher than 300 K has been given by the observation of stimulated emissions due to the strong Coulomb interaction (excitonic gain) from ZnO epilayers [12-14,18]. Moreover, attempts to grow *p*-type ZnO by N-doping have been carried out [16,20,21] and photoluminescence (PL) peaks due to N acceptor have been investigated [20,24,25]. Eventually Tsukazaki and co-workers [26] realized the reproducible growth of N-doped *p*-type ZnO by the repeated-temperature-modulation L-MBE method, and observed UV and visible electroluminescence from a *p*-*n* junction LEDs grown on high-temperature-annealed ZnO self-buffer layers [27] on nearly lattice-matched (0.09% in-plane) (0001) $ScMgAlO_4$ (SCAM)

substrates. However, undoped ZnO usually shows *n*-type conductivity with high residual free electron concentration. The source of free electrons has been attributed to positively charged point defects such as Zn interstitials (Zn_i) and O vacancies (V_O). On the other hand, the role of neutral and negatively charged defects [28] has not been clarified yet. Since quantum efficiency (η) of exciton emissions is determined by radiative and nonradiative recombination lifetimes (τ_r and τ_{nr}, respectively) in a form $\eta=1/(1+\tau_r/\tau_{nr})$, it is an important task to find the origin of nonradiative recombination centers correlating τ_{nr} and defect species, in order to give a way in eliminating those defects to improve η. To comply, a combination of analytical methods of time-resolved PL (TRPL) and positron annihilation methods is effective [29,30].

Positron annihilation [31-36] is an established technique for detecting negatively charged (or neutral) vacancy defects in semiconductors. An implanted positron annihilates with an electron and emits two 511 keV γ-rays, which are broadened due to the momentum component of the annihilating positron-electron pair. Because the momentum distribution of electrons in such defects differs from that in defect-free regions, the defects can be detected by measuring the Doppler broadening spectra of annihilation radiation. The resulting change in the γ-ray spectra is characterized by *S* and *W* parameters [31-35], the former mainly reflects the fraction of annihilating positron-electron pairs of small momentum distribution and the latter represents the fraction of the pairs of large momentum distribution. Since Zn vacancies (V_{Zn}) and their complexes, which have negative charges forming acceptor-type defects in *n*-type ZnO [35], are the most probable candidates of positron trapping centers in ZnO, *S* and *W* can be used as a measure of density / size of V_{Zn}. For multilayer structures, characteristic *S* and positron diffusion length (L_d) in each layer can be determined by using a monoenergetic positron beam [32], by which the mean implantation depth can be adjusted. The analysis [32-36] involves solving the diffusion equation of positrons using initial implantation profile as a function of positron acceleration energy *E*. The value of L_d can be used as a measure of gross density of positron trapping centers (V_{Zn} and V_{Zn}-complexes) plus positron scattering centers (positively charged V_O, Zn_i, O interstitials O_i, and complexes), because both of them shorten L_d [29,35].

Recently, wurzite AlInGaN grown in out-plane nonpolar orientations such as $(1\bar{1}00)$ and $(11\bar{2}0)$ faces are attracting great attention [37,38], since the strained quantum wells (QWs) formed on nonpolar faces do not suffer from the quantum-confined Stark effect (QCSE) due to the polarization fields [39], which severely reduce η in polar (0001) QWs. However, the growth of ZnO in nonpolar orientations is still immature, and little is known about the anisotropic optical transitions in nonpolar ZnO epilayers [40,41].

In this report section, static and dynamic responses of excitons in the bulk and epitaxial ZnO are reviewed to support the fabrication of room-temperature polariton lasers based on ZnO MCs. Following four important topics are treated to view current issues and to indicate a way in improving epilayer qualities: (i) Low temperature OR and photoreflectance (PR) spectra of (0001) ZnO epilayers exhibited distinct exciton-polariton features [41-43] showing that A- and B-exciton resonances dominate the spectra according to the polarization selection rules [1-5] similar to the case for the optical absorption (OA) spectra [44,45]. Low temperature PL spectra of the epilayers grown on SCAM as well as the bulk ZnO single crystal exhibited corresponding excitonic polariton emissions [6,41,43]; values of ω_{LT} for A-, B- and C-exciton polariton branches were obtained to be 1.5, 11.1 and 13.1 meV, respectively. (ii) Using these values and material parameters, Ω_{Rabi} of the model ZnO MC polaritons [8] was calculated to be 191 meV, which is a record high value ever reported for semiconductor MCs, and the value satisfies the requirements to observe the strong exciton-light coupling regime necessary foe polariton lasing above room temperature. (iii) Polarized optical spectra of an out-plane nonpolar $(11\bar{2}0)$ ZnO

epilayer exhibited in-plane anisotropic exciton resonances according to the polarization selection rules for anisotropically strained wurzite material. (iv) PL lifetimes (τ_{PL}) of the films at room temperature were measured by TRPL making a connection with the results of positron annihilation measurement, to correlate the nonradiative recombination centers and point defects. Nonradiative recombination process was found to be governed not by single point defects, but by certain defects introduced with the incorporation of V_{Zn} such as V_{Zn}-defect complexes. Finally, as a result of defect management by growing the films at high T_g followed by subsequent post-growth *in situ* annealing, combined with the use of high-temperature-annealed ZnO self-buffer layers, a record long τ_{nr} for the spontaneous emission as long as 3.8 ns was obtained at room temperature.

Experiment

Samples investigated were (i) undoped bulk ZnO crystal grown by the seeded chemical vapor deposition method [4,6,20,35,46], (ii) an approximately 1-μm-thick undoped $(000\bar{1})$ ZnO epilayer grown by radical-source (RS-) MBE on $(11\bar{2}0)$ Al_2O_3 [19,43], in which the *a*-axis of the epilayer was locked uniaxially, and (iii) 50 nm to 1-μm-thick undoped ZnO epilayers grown by combinatorial L-MBE [26,27,30,35,41] ablating a ZnO single crystal target [46] using a KrF excimer laser. The L-MBE samples were heteroepitaxial $(000\bar{1})$ ZnO on SCAM substrates, homoepitaxial $(000\bar{1})$ ZnO on a ZnO single crystal or on the $(000\bar{1})$ ZnO high-temperature-annealed self-buffer structures prepared on SCAM [27], and a (0001) ZnO on a ZnO single crystal. Typical T_g was between 550 and 1050°C. Some of the samples grown on the self-buffer were annealed during the postgrowth cooling under controlled O_2 ambient pressures. (iv) A nonpolar $(11\bar{2}0)$ ZnO film on $(10\bar{1}2)$ Al_2O_3 was also grown by L-MBE at 650 °C [41], in order to study the effects of anisotropic strains on the band structures. Its in-plane orientation was [0001] ZnO // $[0\bar{1}11]$ Al_2O_3, and the value of full-width at half-maximum (FWHM) of the ZnO $(11\bar{2}0)$ x-ray rocking curve (XRC) was as large as 1100 arcsec. Note that those of ZnO (0002) XRC of polar films were comparable to those of the substrates [27].

OR, PR, PL, photoluminescence excitation (PLE), and TRPL measurements were carried out as a function of temperature. For OR and PR measurements, a white light from a 300 W Xe lamp was focused on a desired face. For the polarized OR, PR, and PL measurements on the bulk ZnO single crystal, both a well-developed $(000\bar{1})$ face and a cleaved $\{11\bar{2}0\}$ face were examined. The incidence angle was smaller than 15°, and that for the PL collection was 0°. Reflected light and PL were polarized using a Glan-Thompson prism polarizer, and were dispersed by a 67-cm-focal-length grating monochromator after passing through a depolarizer. PR and PL spectra were measured using the 325.0 nm line of a cw He-Cd laser as the excitation source. PLE spectra were recorded by monitoring the lower energy tail of the near-band-edge bound exciton emissions (3.355 eV) using a monochromatic light from a 300 W Xe-lamp. The spectral resolution was 0.12 nm (nearly 1 meV at the wavelength of 370 nm) for PR measurement and 0.006 nm (nearly 70 μeV at the wavelength of 370 nm) for OR and PL measurements. Details of the PR, PL, and OR measurement system will be found elsewhere [47]. TRPL measurements were carried out at 293 K using a frequency-doubled mode-locked Ti:Al_2O_3 laser (362.5 nm, 120 nJ/cm^2 per pulse, ~80 fs) and the signal was collected using a standard streak-camera acquisition system. The monoenergetic positron beam line [34,35] was used to determine *S* and *W* parameters as a function of *E*, and L_d was calculated by the fitting using the positron diffusion equation based on the analysis using the algorithm named VEPFIT [36]. The analytical procedures used in this

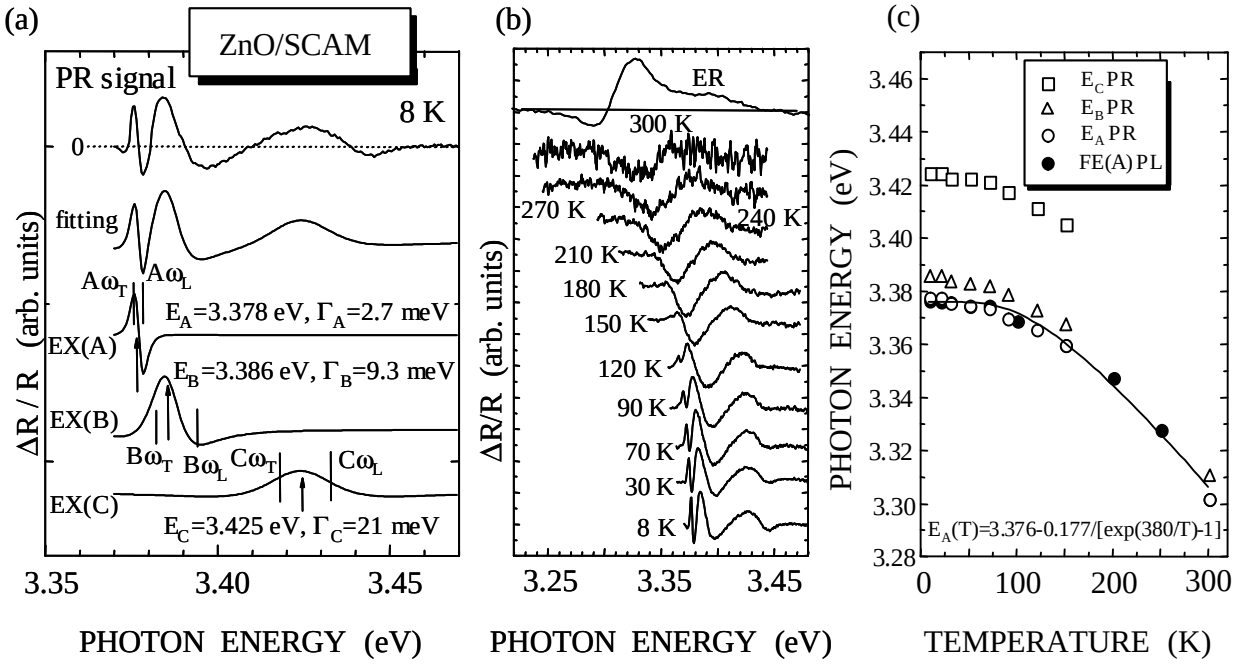

Fig. 1 (a) PR spectrum at 8 K of a 50-nm-thick $(000\bar{1})$ ZnO epilayer on the SCAM substrate (upper trace) after ref. [42]. The second trace shows the fitting result using eq. (1). Bottom three traces labelled EX(A), EX(B) and EX(C) represent A-, B- and C-exciton components, respectively, in which the resonance energies E_α (α=A, B, and C) are shown by the arrows. Vertical lines labelled $\alpha\omega_L$ and $\alpha\omega_T$ show the energies of longitudinal and transverse α-exciton in the strain-free ZnO, respectively, which are taken from ref. [10]. (b) PR spectra and (c) excitonic transition energies as a function of temperature.

study were similar to those described in refs. 34 and 35.

Results and Discussion

PR spectra of a ZnO film grown by L-MBE

In order to determine exciton resonance energies, PR method is known to be useful since it is a contactless form of the electroreflectance (ER) method. The signal is obtained as the change in the reflectivity (ΔR) due to the external light (field) modulation divided by the cw reflectivity (R), and therefore $\Delta R/R$ is proportional to the derivatives of the dielectric function [48]. However, there have been no reported results on the PR spectrum of ZnO until 2002 [42], though ER spectra have been investigated intensively from 1960's [48,49]. PR spectrum at 8 K of a 50-nm-thick $(000\bar{1})$ ZnO epilayer grown by L-MBE on the SCAM substrate is shown by the top trace in fig. 1(a). The spectrum exhibited distinct three resonance structures, and the spectrum was analyzed by the low-field electroreflectance (ER) lineshape function [50]

$$\frac{\Delta R}{R} = \mathrm{Re}\left\{\sum_{j=1}^{p} C_j e^{iq_j}\left[\hbar w - E(j) + i\Gamma_j\right]^{-m_j}\right\}, \qquad (1)$$

where p=3 is the number of the spectral function to be fitted, C_j, θ_j, $E(j)$, and Γ_j are the amplitude, phase, exciton resonance energy, and broadening parameter of the jth feature, respectively. m_j is a parameter that depends on the critical point type. In this study, the value m_j=2 (exciton transition) [50] gave the best fit to experimental data. The fitting result is shown by the second trace in fig.

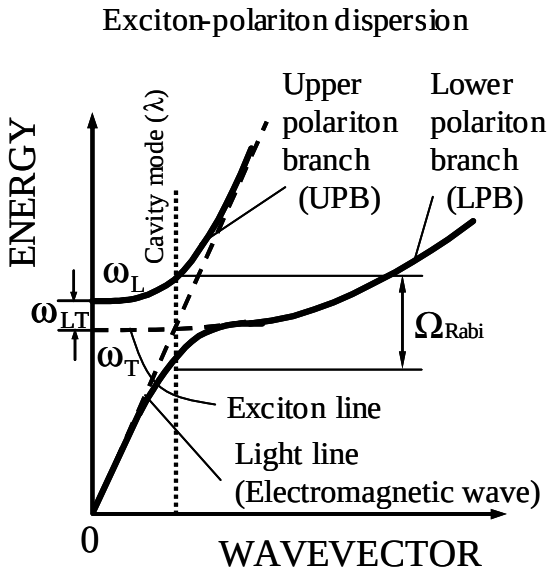

Fig. 2 Dispersion relation of exciton-polaritons. Dashed lines show the dispersion of isolated excitons and light in the material. Longitudinal-transverse splitting of the exciton ω_{LT}, which is the energy difference between ω_L and ω_T at wavevector k=0, represents the stability of exciton-polaritons. If k is locked at the dotted line, the energy difference between UPB and LPB (vacuum field Rabi splitting Ω_{Rabi}) is also locked to have larger value than initial ω_{LT}, indicating that the coupling between the exciton and light became effectively strong.

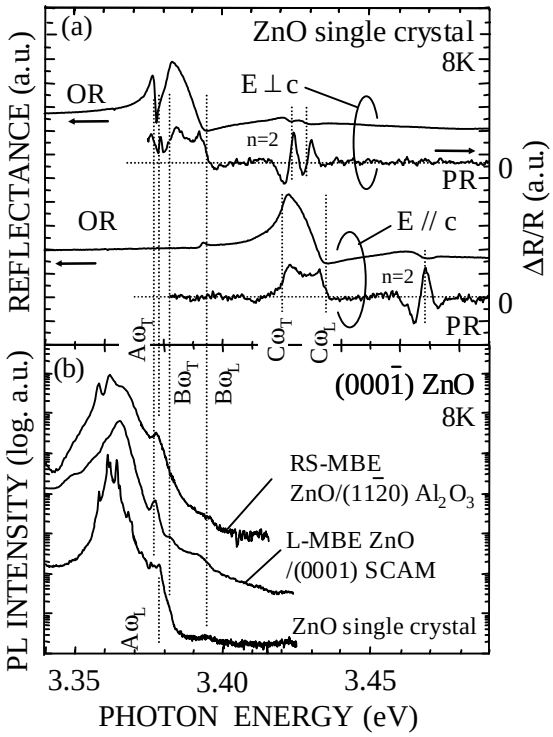

Fig. 3 (a) OR and PR spectra at 8 K of a high quality ZnO single crystal measured under the light polarization $E \perp c$ and E//c, where E is the electric field component and c is the optic axis [6]. $A\omega_T$, $A\omega_L$, $B\omega_T$, $B\omega_L$, $C\omega_T$ and $C\omega_L$ are the energies of transverse and longitudinal A-, B- and C-exciton, respectively. A(n=2) and B(n=2) are resonances due to the first excited states of A- and B-exciton, respectively. (b) PL spectra of the ZnO bulk single crystal [6] and approximately 1-μm-thick (000$\bar{1}$) ZnO epilayers grown by RS-MBE on (11 $\bar{2}$ 0) Al_2O_3 [43] and L-MBE on SCAM substrates [41].

1(a). The bottom three traces labelled EX(A), EX(B), and EX(C) represent A-, B- and C-exciton components, respectively. It should be noted that C-exciton resonance was also observed in the spectrum due to the finite incidence angle of the light. Transition energies were thus obtained to be E_A=3.378 eV, E_B=3.386 eV and E_C=3.425 eV, and the energy positions are indicated by arrows. It should be noted that Γ_B and Γ_C were 9.3 and 21 meV, respectively, which were more than three times larger than Γ_A (2.7 meV). One of the plausible explanations of this was an inhomogeneous distribution of the residual strain, since E_C shifts more rapidly than E_B that itself shifts more rapidly than E_A under strain [51]. However, if whole Γ_B (9.3 meV) was attributed to inhomogeneous distribution of strain, Γ_A and Γ_C are to be 2 and 12 meV, respectively, according to Gil *et al* [51]. Although this effect should not be disregarded, the Γ_C value was too large to be accounted only for the strain inhomogeneity; the broadness of B- and C-transitions was explained considering the contribution by exciton-polaritons, as follows. Note that the dispersion relation of exciton-polariton is depicted in fig. 2. According to Hümmer and Gebhardt [10], ω_{LT} for A-, B- and C-excitons are approximately 2, 11 and 16 meV, respectively. The Γ values obtained in this work nearly agreed with them [10]; ω_L and ω_T for the respective excitonic polaritons in strain-free ZnO [11] are shown by vertical lines in fig. 1(a). Since the epilayer thickness was 50 nm, which was thinner

than the exciton resonance wavelength λ in the material and is not an integer multiplication of λ/2, it may be difficult to pin exciton-polaritons. However, the precursor of polariton formation is considered to be found by the broadening of the respective exciton structures. Note that the large ω_{LT} for B- and C-excitons is indicative of large oscillator strength, since $\omega_{LT}=f_{\perp}\omega_0/\varepsilon_{0\perp}$, where $f_{\perp}$ and $\varepsilon_{0\perp}$ are the oscillator strength and the dielectric tensor component in the plane normal to the optical axis, respectively, and ω_0 is the exciton resonance energy. Indeed, $f_{\perp}$ of B- and C-excitons have been reported to be more than four times that of A-exciton [2].

PR and ER spectra are shown as a function of temperature in fig. 1(b). The PR signal intensity due to A-transition decreased rapidly with the increase in temperature, and the spectra were dominated by B- (and C-) transitions at higher temperatures. The result was consistent with larger $f_{\perp}$ of B- (and C-) excitons. The dependence of E_A and FE(A), the latter being free A-exciton emission peak energy, on temperature can be fitted by the Bose-Einstein statistics, as shown by the solid curve in fig. 1(c) giving an Einstein characteristic temperature Θ_E of 380 K (33 meV or 268 cm^{-1}). This value is in good agreement with the energy maximum of the low-energy group of bulk phonon density of states (8THz=33 meV or 380 K) [52].

Exciton-polaritons in ZnO

Polarized OR and PR spectra and PL spectra at 8 K of a high quality ZnO single crystal [43] are shown in figs. 3(a) and 3(b), respectively [6]. For $E\perp c$, the OR spectrum exhibited strong anomalies around 3.38 and 3.39 eV, which are due to the ground state (n=1) A- and B-excitons, respectively. In addition, remarkable anomalies were observed at around 3.42 and 3.43 eV, which were assigned to the first excited states (n=2) of A and B-excitons, respectively. In the figure, positions of ω_T and ω_L for A-, B- and C-excitonic polaritons [11] are drawn by vertical dotted lines (labeled $A\omega_T$, $A\omega_L$, $B\omega_T$, $B\omega_L$, $C\omega_T$, and $C\omega_L$). Obviously, the PR spectrum exhibited fairly noisy but fine structures at those energies, implying a formation of exciton-polaritons. The PR signal $\Delta R/R$ given by eq. (1) is deduced as [48-50]

$$\frac{\Delta R}{R}=\mathrm{Re}\left\{\frac{2n_a}{n(e-e_a)}\right\}=\mathrm{Re}\{(a-ib)\Delta e\}=a\Delta e_1+b\Delta e_2, \tag{2}$$

where $n^2=\varepsilon$, $n_a^2=\varepsilon_a$, n_a is the real part of the refractive index, $\Delta\varepsilon=\Delta\varepsilon_1+i\Delta\varepsilon_2$ is the perturbation-

Table 1: Exciton-polariton parameters in ZnO single crystal determined by the OR measurements [6] and those in free-standing GaN [53,54] prepared by lateral epitaxial overgrowth technique and subsequent substrate polishing [62].

Exciton	Polarization	ZnO (meV) [6]					GaN (meV) [54]		
		n=1			n=2	E_{ex}			
		ω_T	ω_L	ω_{LT}			ω_T	ω_{LT}	E_{ex}
A (Γ_9)	$\perp$	3376.8	3378.3	1.5	3423.1	60	3479.1	1.34	23.44
B (Γ_7)	$\perp$ (//)	3383.0	3394.1	11.1	3429.0	53	3484.4	1.17	23.6
C (Γ_7)	// ($\perp$)	3348.4	3435.3	13.9	3467.9	49	3502.7	0.27	(20.3)

induced change in the dielectric function ε, and α and β are the Seraphin coefficients. Equation (2) implies that the signal $\Delta R/R$ is purely sensitive to $\Delta\varepsilon$; i.e. PR method monitors exciton resonances in wide bandgap materials. Therefore, observation of exciton-polaritons by the PR method [6,42,43,47,53,54] is reasonable since they represent a coupled state between an electromagnetic wave and excitons. The value of ω_{LT} for the B-excitonic polariton was confirmed as large as 11.1 meV, implying the large oscillator strength. The energies obtained from fig. 3 are summarized in table 1, together with the data obtained for GaN [54]. For *E*//*c*, the OR spectrum exhibited a strong and a weak anomalies around 3.43 and 3.47 eV, which are due to n=1 and n=2 C-exciton resonances, respectively. As is the case with A- and B-excitons, PR signal exhibited fine structures at $C\omega_T$ and $C\omega_L$, giving the ω_{LT} of C-exciton as large as 13.9 meV. From these values, the spin-orbit splitting and crystal field splitting were estimated by the quasi-cubic model [3] to be 14 and 48 meV, respectively.

PL spectra of the ZnO bulk single crystal [6] and approximately 1-μm-thick $(000\bar{1})$ ZnO epilayers grown by RS-MBE on $(11\bar{2}0)$ Al_2O_3 [43] and L-MBE on SCAM [41] are shown in fig. 3(b) where logarithmic *y*-axis is used. Sharp PL lines between 3.355 and 3.372 eV observed in the bulk single crystal (bottom trace) have been assigned to a series of bound exciton complex recombination emissions. Detailed studies on these lines have been carried out by several researchers [4,20,25,46]. In addition, the PL spectrum exhibited a weak but noticeable peak at 3.3941 eV and a shoulder at 3.3830 eV. They were assigned as being due to the emission of $B\omega_L$ and $B\omega_T$, respectively, since the energy agreed with those determined from the OR and PR spectra. Although the picture is not clear, PL peaks at 3.3783, 3.3765 and 3.3755 eV were found in the bottom spectrum [6]. They were essentially polarized to $E\perp c$ and were assigned to the emission of $A\omega_L$ and $A\omega_T$ and a bound exciton, respectively, judging from the energy positions [6]. Observation of these exciton-polariton emissions imply that the ZnO single crystal was of good quality. Since the exciton-polariton emissions were also found in the improved ZnO epilayers, as shown in fig. 3(b), and the fabrication of *p*-*n* junction LEDs was realized [26], epitaxial formation of ZnO-based MCs [8] are now considered to be possible.

The calculated exciton-polariton dispersion in the model MC described below is shown in fig. 4(a). The calculation procedure was the same as that carried out in ref. [8] except for

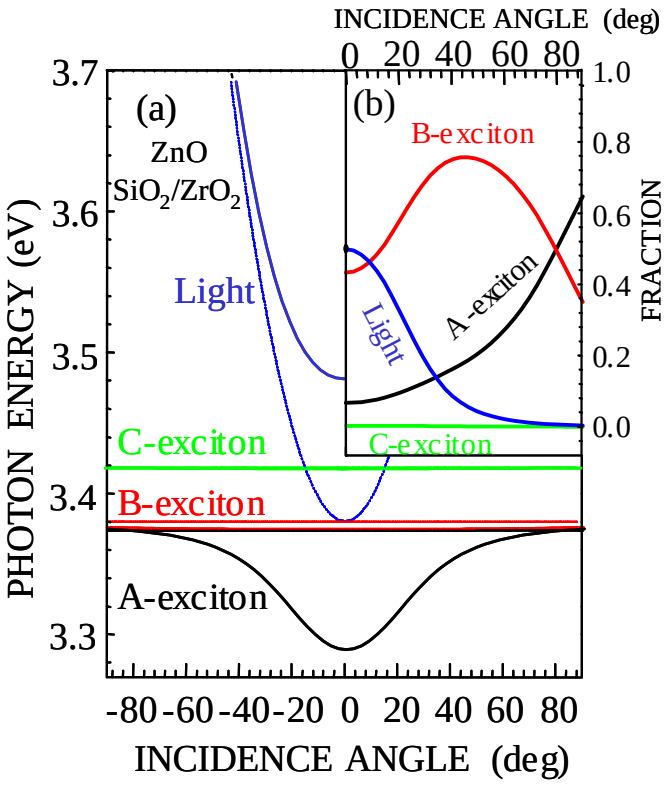

Fig. 4 Eigenenergies of the ZnO cavity modes versus the incidence angle. Dotted lines indicate the positions of the unperturbed modes: "Light" indicates the light mode, and A-, B- and C-exciton indicate the A-, B- and C-exciton resonances in ZnO, respectively. The inset shows the percentage of the excitonic components and the photonic component in the eigenmode of the lowest cavity-polariton state versus the in-plane wave vector.

eigenenergies of A-, B- and C-excitons and the cavity structure. The model MC considered herein consisted of the λ cavity of ZnO sandwiched between 8 pairs of SiO_2/ZrO_2 and 7 pairs of ZrO_2/SiO_2 dielectric distributed Bragg reflectors (DBRs) of quarter-wavelength layers in the bottom and top mirrors, respectively. SiO_2 was assumed as a substrate. The cavity photon mode was placed at 3.383 eV (366.5 nm in vacuum) at zero detuning from the B exciton resonance, since the B-exciton has a large ω_{LT} of 11.1 meV and polarized to $E \perp c$. Refractive indices of ZnO, SiO_2, and ZrO_2 at 366.5 nm were taken as 2 [55], 1.48 [56], and 2.1 [57], respectively. The ZnO, SiO_2, and ZrO_2 layer thicknesses were 183.2, 61.9, and 44.7 nm, respectively. In fig.4, four branches arising from A-, B- and C-exciton resonances and the cavity light mode (denoted by "Light") are shown. Dotted thin lines indicate the positions of the corresponding unperturbed modes. Among those, the lowest polariton branch is of the highest interest for realization of polariton Bose condensation and lasing. The inset shows the percentage of the excitonic components and the photonic component in the eigenmode of the lowest cavity-coupled polariton state as a function of in-plane wave vector.

Important findings are following. (I) Zero wavevector is locked by the cavity at which unperturbed B-exciton resonance and light line crossover (shown by dotted line in fig. 2), leading to the increase in Ω_{Rabi} up to 191 meV due to the enhanced coupling between B-exciton and light modes. This value is the highest value ever recorded for semiconductor MCs. The difference between the present value and that calculated by Zamfirescu *et al*. (120 meV) [8] arose from the change in ω_{LT} values of excitons, presumably due to the experimental determination of the resonance energies. (II) The eigenfunction of the fundamental state at zero incidence angle has less than 50% of the photonic component (see the inset), which is essential for efficient polariton relaxation toward the ground state through scattering of the excitonic component with acoustic phonons, other excitons, and free carriers introduced in the cavity. (III) The fundamental state has 40% B-excitonic character at zero incidence angle and it increases to 80% for the incidence angle of 40°. The results (II) and (III) mean that B-excitonic character is strongly reflected to the lowest polariton branch denoted by "A-exciton" in fig. 4 [8], in which Bose condensation of polaritons is expected in a cavity polariton laser structure [9]. Using the values listed in table 1 and polariton dispersion relation given in fig. 4, the critical density of formation of Bose condensation of exciton-polaritons in the model MC was calculated as a function of temperature. As a result, critical temperature of 610 K was given from the exciton dissociation energy, and allowable exciton density between 1×10^{12} cm^{-2} and 7×10^{13} cm^{-2} at 300 K were obtained due to the large electron-hole plasma density to screen excitons (Mott density for excitons). By using progressively improving epitaxial growth methods, polariton laser effect due to Bose condensation will probably be observed at room temperature in the near future.

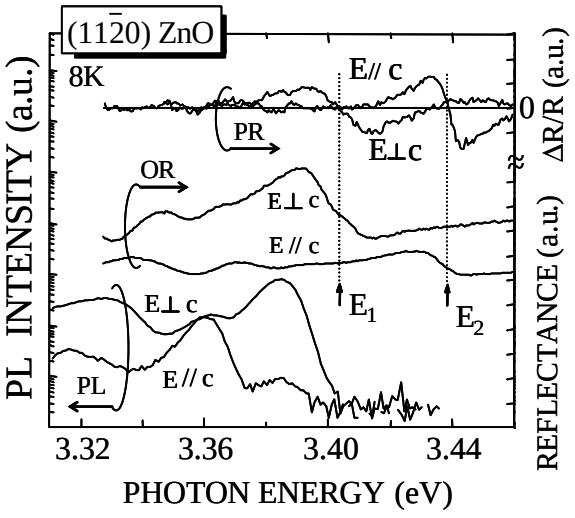

Fig. 5 Polarized PR, OR, and PL spectra at 8 K of the (11$\bar{2}$0) ZnO epilayer grown on (10$\bar{1}$2) Al_2O_3 grown by L-MBE at 650 °C [41]. E_1 and E_2 represent the energies of exciton transitions observed for $E \perp c$ and E//c, respectively, in OR and PR spectra.

Excitons in nonpolar face ZnO

Table 2: Exciton parameters in anisotropically-strained $(11\bar{2}0)$ ZnO and nearly strain-free $(000\bar{1})$ and (0001) ZnO epilayers at 8 K.

Strained $(11\bar{2}0)$ ZnO			Nearly strain-free (0001) and (0001) ZnO		
Exciton[a]	Polarization[b]	Energy (eV)	Exciton	Polarization	Energy (eV)
E_1	E//$[1\bar{1}00]$	3.402	A	$E\perp$[0001]	3.377
E_2	E//[0001]	3.439	B	$E\perp$[0001]	3.383(T),3.393(L)
E_3	E//$[11\bar{2}0]$	Not allowed	C	E//[0001]	-

[a] Notation according to ref. [58]

[b] Calculation according to ref. [58]

Polarized OR and PR spectra of an out-plane nonpolar $(11\bar{2}0)$ ZnO epilayer grown by L-MBE exhibited anisotropic exciton resonance structures [41] according to the polarization selection rules for anisotropically-strained wurzite material [58], as follows. Polarized PR, OR, and PL spectra of $(11\bar{2}0)$ ZnO measured at 8 K are shown in fig, 5. The PR and OR spectra exhibited excitonic resonance structures at 3.402 eV and 3.439 eV for $E\perp c$ and $E//c$, respectively. These energies were higher than those of A- (or B-) and C-excitons in strain-free ZnO [1-6,59]. The energy shift is due to anisotropic strains [58] caused by the lattice and thermal expansion mismatches. The strains are quantified by x-ray diffraction (XRD) measurements to be -0.41%, -0.19% and +0.49% along $[1\bar{1}00]$, [0001] and $[11\bar{2}0]$ directions, respectively, where minus and plus signs represent compressive and tensile, respectively. Since these anisotropic strains change the crystal symmetry from C_{6v} to C_{2v}, the labels A, B and C can no longer be used. Therefore, nomenclature E_1, E_2 and E_3 for the ground state of the three excitons are used, as Ghosh *et al.* [58] have used to describe exciton structures in nonpolar $(1\bar{1}00)$ GaN. They have calculated the oscillator strengths and transition energies of excitons in anisotropically-strained GaN [58], which has C_{6v} symmetry and valence band ordering of A-Γ_9, B-Γ_7 and C-Γ_7. According to their calculation, E_1, E_2 and E_3 excitons in our strained $(11\bar{2}0)$ ZnO are predominantly polarized to $[1\bar{1}00]$, [0001] and $[11\bar{2}0]$, respectively. Therefore, transition structures observed under $E\perp c$ (3.402 eV) and $E//c$ (3.439 eV) are assigned to E_1 and E_2 transitions, respectively, as shown in table 2. The E_3 transition is not observed, since the $[11\bar{2}0]$ direction is normal to the surface. Consistent with the polarization selection rules for the E_1 transition, a near-band-edge PL peak at 3.384 eV in the $(11\bar{2}0)$ ZnO film is polarized to $E\perp c$ (parallel to $[1\bar{1}00]$). Because the peak energy is lower by 18 meV than the E_1 transition energy, the peak is tentatively assigned to I_6 peak (3.36 eV in strain-free ZnO) [60], which has been assigned to the recombination of excitons bound to a neutral Al donor [59]. From the fact that state-of-the-art nearly strain-free $(000\bar{1})$ and (0001) ZnO films grown by L-MBE exhibit free exciton emissions and exciton-polariton emissions [27,41], as shown in fig. 3, residual anisotropic and inhomogeneous strains in the $(11\bar{2}0)$ ZnO film are considered to degrade the electronic quality to observe free excitons and simultaneously to cause the broadening of FWHM values of XRD and PL peaks. Therefore, a lattice and thermally-

matched substrate is necessary to further improve the exciton spectra of the $(11\bar{2}0)$ ZnO epilayers. Nevertheless, the observation of correct in-plane polarization of the exciton transitions is encouraging in designing $(11\bar{2}0)$ or $(1\bar{1}00)$ nonpolar face devices using epitaxial ZnO grown in nonpolar orientations, as is the case AlInGaN materials [37,38,58,61].

Exciton dynamics and point defects in ZnO epilayers

In order to improve overall epilayer qualities for the realization of high η LEDs using *p*-type ZnO, it is an important task to figure out the origin of nonradiative recombination centers correlating τ_{nr} and defect species. To complete this purpose, a combination of analytical methods of TRPL and monoenergetic positron annihilation methods have been carried out [29,30,35,41]. Representative TRPL signals of the near-band-edge emission at 3.3 eV, which has been assigned to the free exciton emission, for the ZnO single crystal and ZnO epilayers grown by L-MBE on SCAM measured at 293 K are shown in fig. 6(a) and 6(b), respectively [30]. The bulk ZnO exhibited a biexponential decay having long lifetimes of the order of 1 and 14 ns for the fast and slow components, respectively. Both of them represent nonradiative recombination lifetimes originating from two different nonradiative pathways. Note that the value 970 ps was comparable to that of GaN single crystal being 860 ps [29,62], suggesting that the material contained small number of nonradiative defects. On the other hand, the epilayers showed a single exponential decay with much shorter lifetimes. Because τ_{PL} at 293 K is in general dominated by τ_{nr} due to the activation of nonradiative defects, short τ_{PL} values for the epilayers suggested the presence of higher density nonradiative defects compared with the bulk crystal at that time [30,41].

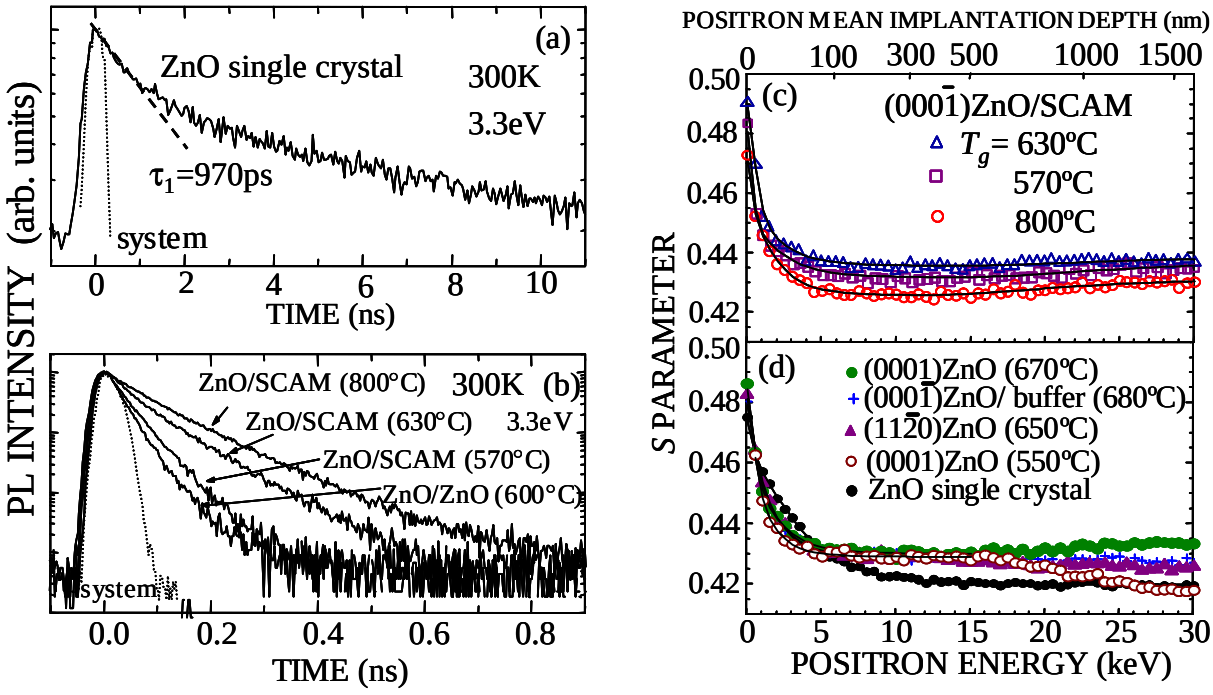

Fig. 6 Representative TRPL signals of the near-band-edge emission at 3.3 eV for (a) the ZnO single crystal and (b) L-MBE films measured at 293 K. Doppler broadening *S* parameter of (c) heteroepitaxial $(000\bar{1})$ ZnO layers on SCAM and (d) homoepitaxial {0001} ZnO films and heteroepitaxial nonpolar $(11\bar{2}0)$ ZnO epilayer on $(10\bar{1}2)$ Al_2O_3 as a function of incident positron energy *E*. The solid curves in (c) and (d) show the results of fitting the experimental data.

Nevertheless, nonradiative defect density in ZnO/SCAM was considered to be reduced by increasing T_g, because τ_{PL} increased with the increase in T_g, as shown in fig. 6(b).

S parameter of heteroepitaxial $(000\bar{1})$ ZnO layers on SCAM and that in homoepitaxial {0001} ZnO films and nonpolar $(11\bar{2}0)$ ZnO epilayer are shown as a function of incident positron energy *E* in figs. 6(c) and 6(d), respectively [30,35]. The mean implantation depth of positrons is shown in the upper horizontal axis. The increase in *S* at low *E* (≅0 keV) is due to the annihilation of positrons and positronium atoms at the surface, and the *S* values at high *E* (≥20 keV) include the information of the substrate. The constant *S* values for *E* = 10-15 keV mean that most of positrons annihilate in the films. Solid curves show the fitting results [35] of positron diffusion equation. The fitting curves well reproduced the experimental data, and the values of *S* and L_d are shown as a function of τ_{PL} at 293 K obtained by TRPL in fig. 7: in fig. 7, sample identification is written in the order of growth direction, T_g, and substrate material. The values of L_d for both the epilayers and the bulk crystal were much shorter than the typical one (about 200-300 nm) in nearly defect-free materials such as Si [63] and GaAs [64] and close to that in very low threading dislocation density GaN [34]. As shown in fig. 7, all the epilayers exhibited larger *S* and shorter L_d compared with those of the bulk crystal, indicating the presence of larger number (greater size) positron trapping centers (neutral and negatively-charged V_{Zn} and V_{Zn} complexes) and positron scattering centers (positively charged V_O, Zn_i, O_i, and complexes). For ZnO/SCAM, *S* tended to decrease with the increase in T_g [30] and the smallest value was obtained from the film grown at 800°C, although L_d was the shortest: the homoepitaxial layers exhibited smaller *S* parameters but relatively short L_d [30]. From the results, the increase in T_g and lattice matching were considered to be effective in reducing *S* parameter (V_{Zn} density). This observation was consistent with the reduction of nonradiative defect density with increasing T_g for ZnO/SCAM, which was concluded from the results of TRPL measurements, as revealed from figs. 6(b) and 6(c). It should be noted from fig. 6(d) that *S* parameters of (0001) homoepitaxial films and $(11\bar{2}0)$ film were comparable to those of $(000\bar{1})$ homoepitaxial films. The results implied that the growth polar direction had negligible influence on the incorporation of V_{Zn}, the result being different from the case for GaN that incorporation of impurities [65] as well as V_{Ga} and V_{Ga}-O defect complexes was enormously enhanced for the $[000\bar{1}]$ polar growth [34].

To discuss the origin of nonradiative defects exist in unintentionally doped ZnO, τ_{PL} at 293 K, which is the representative of τ_{nr}, is plotted as functions of *S* and L_d in figs. 7(a) and 7(b), respectively. As shown, the nonradiative lifetime increased with the decrease in *S* and the increase in L_d. The former means

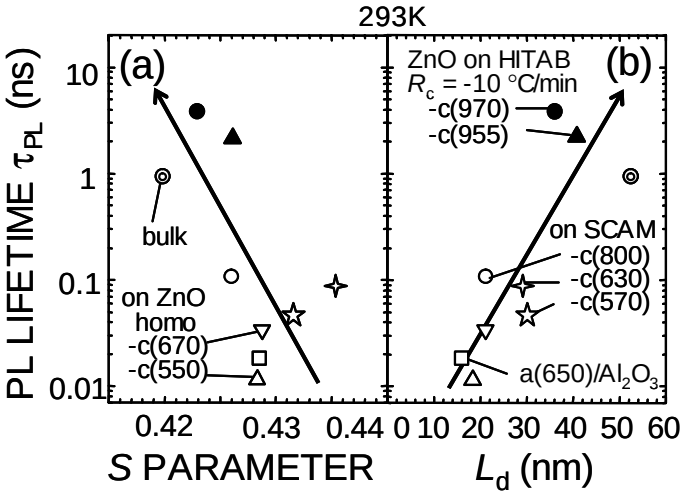

Fig. 7 TRPL decay constants of the near-band-edge excitonic PL peak at 293 K, which in general determine the time-integrated intensity at room temperature, in the bulk, heteroepitaxial, and homoepitaxial ZnO as functions of (a) *S* parameter and (b) L_d. Sample identification is written in the order of growth direction, T_g in bracket, and substrate material.

the reduction in V_{Zn}-related negatively charged defect density and the latter means the reduction in gross density of positively charged, negatively charged, and neutral point defects. Because τ_{nr} did not have a perfect correlation with T_g or growth orientations, the dominant parameter that limits τ_{nr} and thereby emission efficiency η at 300 K must be the gross density of point defects, which are incorporated with V_{Zn} and may be localized around structural defects. Certain defects such as V_{Zn}-defect complexes are the most probable candidates. Here we should mention that TRPL measurements were carried out by monitoring the near-band-edge excitonic PL peak, and therefore τ_{PL} includes both the real τ_{nr} and carrier transfer time to deep defect levels such as V_O, Zn_i, V_{Zn} and V_{Zn}-defect complexes. Apparently, some of them are radiative defects (origin of green luminescence band: GL), but they reduce the experimental τ_{nr}. However, there exist other V_{Zn}-defect nonradiative recombination centers, since τ_{nr} of the samples that do not exhibit GL band also obeyed the tendency shown in fig. 7.

Elimination of point defects as a fundamental pathway in improving quantum efficiency of excitonic emissions in ZnO epilayers

From figs. 6(b) and 7, τ_{nr} was found to increase with increasing T_g for ZnO/SCAM samples. In order to tremendously improve η in ZnO epilayers at 300 K, high-temperature growth experiments were carried out using the high-temperature-annealed ZnO self-buffer layers [27] on SCAM substrates, since T_g of the sample sets shown in figs. 6 and 7 was much lower than typical one for GaN growth (typically 1050-1100 °C [39]). Details of the self-buffer preparation procedure has been given in ref. [27]. Because L_d of ZnO/SCAM grown at 800 °C was shorter than those grown around 600 °C (but S was smaller), as shown in fig. 7, nonequilibrium incorporation of positron scattering centers such as interstitials and V_O was probable during higher temperature growth. To suppress the enhanced incorporation of those positively charged defects, postgrowth annealing was carried out simultaneously. Values of τ_{PL} at 293 K of 500-1000-nm-thick ZnO films are plotted as functions of T_g, cooling rate, and ambient O_2 pressure during cooling in fig. 8. Note that excitation power for the TRPL measurements was reduced to 120 nJ/cm^2 per pulse to realize weak excitation regime, in which exciton density would be lower than overall nonradiative defect density to compare τ_{nr}, since τ_r of electron-hole plasma is much shorter than that of exciton spontaneous emission. As shown, τ_{nr} tended to increase with the increase in T_g and decrease in cooling rate and ambient O_2 pressure. The value reached up to 3.8 ns for T_g=1020 °C and cooled at 10 °C/min in 10^{-6} Torr O_2 ambient. This value is the longest spontaneous emission lifetime at room temperature ever recorded in ZnO. These results imply that for intermediate T_g up to 1000 °C, those interstitials out-diffused during postgrowth cooling under near vacuum. Indeed, L_d of the samples exhibiting long τ_{nr} increased

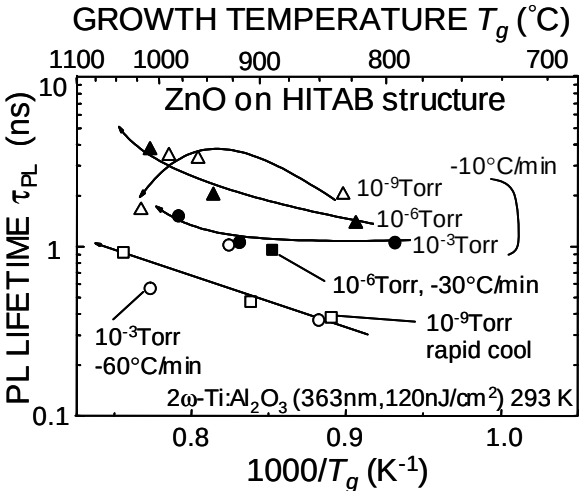

Fig. 8 TRPL decay constants of the near-band-edge excitonic PL peak at 293 K, which in general determine the time-integrated intensity at room temperature, in ZnO epilayers grown on HITAB ZnO [27]. The epilayers were annealed during cooling after the growth under different cooling rates and ambient O_2 pressures.

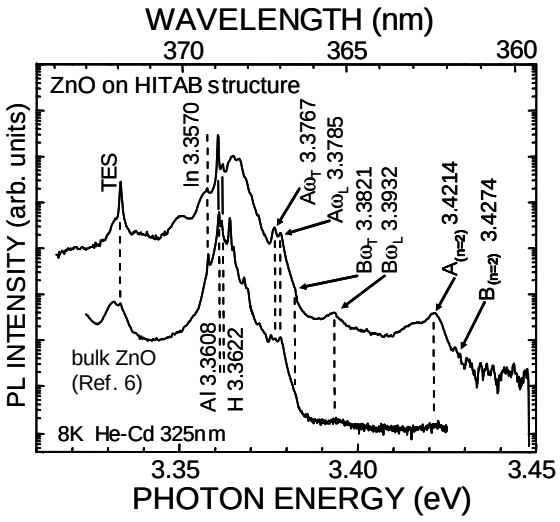

Fig. 9 Representative PL spectrum at 8K of the ZnO epilayer grown on HITAB structure (T_g= 850°C, R_c=-10°C/min., P_{O2}=10^{-6} Torr). For comparison, PL spectrum of the bulk ZnO single crystal measured at 8 K is also shown (after Ref. [6])

excited using the 325.0 nm line of a cw He-Cd laser (2 mW), at 8 K of the improved ZnO epilayer grown on the HITAB structure (T_g=850 °C, R_c=-10 °C/min., P_{O2}=10^{-6} Torr) is shown in Fig. 9. As shown, rich structures due to excitons were observed; sharp PL lines between 3.35 and 3.374 eV due to the recombination of excitons bound to neutral H, Al, In, and other impurities and defects [59]; two-electron satellites (TES) at around 3.332 eV [20]; clearly split peaks between 3.376 and 3.394 eV due to lower and upper polariton branches (transverse and longitudinal excitons) of A- and B-excitons ($A\omega_T$, $A\omega_L$, $B\omega_T$, and $B\omega_L$); recombination of the excited states of free A- and B-excitons [$A_{(n=2)}$ and $B_{(n=2)}$] and bound excitons around 3.42 eV. These rich exciton features have never been reported for ZnO epitaxial layers grown by a variety of methods, indicating the excellent quality of the present epilayers.

TRPL signal measured at the NBE peak energy of the same sample is shown as a function of temperature (T) in Fig. 10(a). To visualize the improved η_{int}, which is defined as the PL intensity at particular T divided by that at 8 K, spectrally-integrated normalized up to 50 nm or longer (the film thickness of approximately 1 μm was too thin to obtain the "flat" region in the *S-E* curve), which is comparable to that in the bulk ZnO. For the lowest O_2 pressure of 10^{-9} Torr (background O_2 in the chamber), the annealing higher than 1000 °C caused the decrease in τ_{nr}, which may be due to additional introduction of vacancy-type point defects and dissociation of ZnO epilayers. A possibility to improve τ_{nr} and hence η of exciton emissions at room temperature was shown using high T_g and appropriate defect management. Since *p*-type ZnO was realized using the repeated temperature modulation epitaxy [26], in which N atoms were doped at low T_g and the crystal quality was recovered during subsequent high T_g growth, this defect management technique will enable to observe polariton laser effect in the near future.

High-resolution PL spectrum, which was

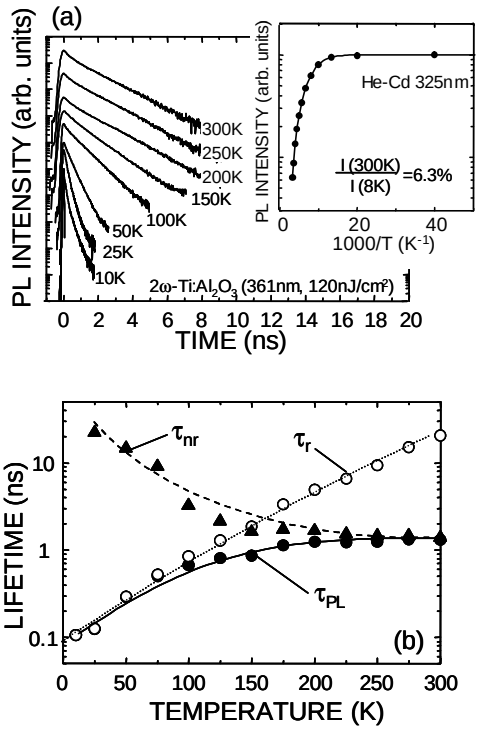

Fig. 10 (a) TRPL signal monitored at the NBE PL peak energy of the ZnO epilayer grown on the HITAB structure (T_g=850°C, R_c=-10°C/min., P_{O2}=10^{-6} Torr) as a function of temperature (T). The inset shows the spectrally integrated NBE PL intensity as a function of 1/T. At 300 K, η_{int} was 6.3%. (b) Values of τ_{PL}, τ_r, and τ_{nr} as a function of T; τ_r and τ_{nr} were derived from τ_{PL} and η_{int}.

PL intensity is plotted as a function of $1/T$ in the inset. The TRPL signal exhibited nearly single exponential decay shape, and τ_{PL} increased with the increase in T from 10 to 275 K; the value of τ_{PL} is plotted as a function of T in Fig. 10(b). This observation that η_{int} decreased but τ_{PL} increased with T means that the radiative lifetime (τ_r) dominated τ_{PL} up to relatively high temperatures. The values of τ_r and τ_{nr} were deduced from τ_{PL} and η_{int} using the relations $\eta_{int}=1/(1+\tau_r/\tau_{nr})$ and $1/\tau_{PL} = 1/\tau_r+1/\tau_{nr}$, and are plotted in Fig. 10(b). Indeed, the critical temperature at which τ_r and τ_{nr} crossover was as high as 160 K, and long τ_{nr} (1.31 ns) was obtained at 300 K. It should be noted that η_{int} was 6.3% at 300 K, which is approximately an order of magnitude higher than the typical value reported for low dislocation density GaN [62] prepared by lateral epitaxial overgrowth techniques.

Conclusions

Static and dynamic responses of excitons in state-of-the-art bulk and epitaxial ZnO were reviewed to support the possible realization of polariton lasers. Following four important topics were treated to view current issues and to indicate a way in improving epilayer qualities: (i) Exciton-polariton structures in bulk and epitaxial ZnO were resolved at 8 K, and the energies of PR resonances corresponded to those of UPB and LPB, where A-, B- and C-excitons couple simultaneously to an electromagnetic wave. PL peaks due to the corresponding polariton branches were observed, and ω_{LT} of the corresponding excitons were obtained to be 1.5, 11.1, and 13.1 meV, respectively. The latter two values are more than two orders of magnitude greater than that of GaAs being 0.08 meV. (ii) Using those values and material parameters, corresponding Ω_{Rabi} of exciton-polaritons coupled to a model MC mode was calculated to be 191 meV, which is a record high value ever reported for semiconductor MCs. The value satisfies the requirements to observe strong exciton-light coupling regime necessary for polariton lasing above room temperature. (iii) Polarized OR and PR spectra of an out-plane nonpolar $(11\bar{2}0)$ ZnO epilayer were measured, because ZnO QWs grown in nonpolar orientations are expected to show higher emission efficiencies due to the elimination of spontaneous and piezoelectric polarization fields normal to the QW plane. They exhibited in-plane anisotropic exciton resonances according to the polarization selection rules for anisotropically-strained wurzite material. (iv) Impacts of point defects on the nonradiative processes in L-MBE ZnO were studied: free excitonic PL intensity at room temperature naturally increased with the increase in τ_{nr}. The value of τ_{nr} increased and density or size of V_{Zn} defects decreased with the increase in T_g in heteroepitaxial films grown on SCAM substrate, and the use of homoepitaxial substrates further reduced V_{Zn} density. The value of τ_{nr} was shown to increase with the decrease in gross density of positively and negatively charged and neutral point defects including complexes rather than with the decrease in V_{Zn} density. The results indicate that nonradiative recombination process is governed not by single point defects, but by certain defects introduced with the incorporation of V_{Zn}, such as V_{Zn}-defect complexes. As a result of defect elimination by growing the films at high T_g followed by subsequent post-growth *in situ* annealing, combined with the use of HITAB ZnO, a record long τ_{nr} for the spontaneous emission as long as 3.8 ns was obtained at room temperature. Also, rich structures due to longitudinal-transverse splitting of exciton-polaritons and excited states of excitons were found in the low-temperature PL spectrum of the epilayer that exhibited η_{int}=6.3% at 300 K. By using progressively improving epitaxial growth methods, polariton laser effect due to Bose condensation will be observed at room temperature in the near future.

Acknowledgments

The authors would like to thank Prof. A. Kavokin, Prof. B. Gil, Prof. H. Koinuma, Prof. Y. Segawa, and Prof. Emeritus T. Kouda for fruitful discussions

References

[1] Hümmer K 1973 *Phys. Stat. Sol.* **56** 249.
[2] Thomas D G 1960 *J. Phys. Chem. Solids* **15** 86.
[3] Hopfield JJ 1960 *J. Phys. Chem. Solids* **15** 97.
[4] Reynolds D, Look D C, Jogai B, Litton C W, Cantwell G, and Harsch W 1999 *Phys. Rev*. B **60** 2340.
[5] Gil B 2001 *Phys. Rev*. B **64** 201310R.
[6] Chichibu S F, Sota T, Cantwell G, Eason D B, and Litton C W 2003 *J. Appl. Phys*. **93** 756.
[7] Weisbuch C, Nishioka M, Ishikawa A, and Arakawa Y 1992 *Phys. Rev. Lett.* **69** 3314.
[8] Zamfirescu M, Kavokin A, Gil B, Malpuech G, and Kaliteevski M 2002 *Phys. Rev.* B **65** 161205R.
[9] Imamoglu A, Ram R J, Pau S and Yamamoto Y 1996*Phys. Rev.* A **53** 4250.
[10] Hümmer K and Gebhardt P 1978 *Phys. Stat. Sol.* (b) **85** 271.
[11] Lagois J 1981 *Phys. Rev*. B **23** 5511.
[12] Yu P, Tang Z, Wong G, Kawasaki M, Ohtomo A, Koinuma H, and Segawa Y 1996 *Proc. 23rd Int'l Conf. on Physics of Semicond.*, Berlin, ed M Scheffler and R Zimmermann (Singapore: World Scientific), vol. 2, p. 1453.
[13] Yu P, Tang Z, Wong G, Kawasaki M, Ohtomo A, Koinuma H, and Segawa Y 1997 *Solid State Commun*. **103** 459.
[14] Ohtomo A, Kawasaki M, Sakurai Y, Yoshida Y, Koinuma H, Yu P, Tang Z, Wong G, and Segawa Y 1998 *Mater. Sci. Eng*. **54** 24.
[15] Choopun S, Vispute R, Noch W, Balsamo A, Sharma R, Venkatesan T, Iliadis A, and Look D C 1999 *Appl. Phys. Lett*. **75** 3947.
[16] Joseph M, Tabata H, and Kawai T 1999 *Jpn. J. Appl. Phys*. **38** L1205.
[17] Cook J and Schetzina F 1996 *J. Electron. Mater*. **25** 855.
[18] Bagnall D, Chen Y, Zhu Z, Yao T, Koyama S, Shen M, and Goto T 1997 *Appl. Phys. Lett*. **70** 2230; 1998 *ibid* **73** 1038.
[19] Iwata K, Fons P, Yamada A, Matsubara K, and Niki S 2000 *J. Cryst. Growth* **209** 526.
[20] Look D C, Reynolds D C, Litton C W, Jones R L,Eason D B, and Gantwell G 2002 *Appl. Phys. Lett*. **81** 1830.
[21] Minegishi K, Koiwai Y, Kikuchi Y, Yano K, Kasuga M, and Shimizu A 1997 *Jpn. J. Appl. Phys*. **36** L1453.
[22] Ogata K, Kawanishi T, Maejima K, Sakurai K, Fujita Sz, and Fujita Sg 2001 *Jpn. J. Appl. Phys*. **40** L657.
[23] Chichibu S F, Yoshida T, Onuma T, and Nakanishi H 2002 *J. Appl. Phys*.**91** 874.
[24] Tamura T, Makino T, Tsukazaki A, Sumiya M, Fuke S, Furumochi T, Lippmaa M, Chia C H, Segawa Y, Koinuma H, and Kawasaki M 2003 *Solid State Commun*. **127** 265.
[25] Strassburg M, Rodina A, Dworzak M, Haboeck U, Krestnikov I L, Hoffmann A, Gelhausen O, Phillips M R, Alves H R, Zeuner A, Hofmann D M, and Meyer B K 2004 *Phys. Stat. Sol.* (b) **241** 607.
[26] Tsukazaki A, Ohtomo A, Onuma T, Ohtani M, Makino T, Sumiya M, Ohtani K, Chichibu S F, Fuke S, Segawa Y, Ohno H, Koinuma H, and Kawasaki M 2005 Nature Materials **4** 42.
[27] Tsukazaki A, Ohtomo A, Yoshida S, Kawasaki M, Chia C H, Makino T, Segawa Y, Koida T, Chichibu S F, and Koinuma H 2003 *Appl. Phys. Lett*. **83** 2784.

[28] Kohan A F, Ceder G, Morgan D, and Van de Walle C G 2000 *Phys. Rev*. B **61** 15019.
[29] Chichibu S F, Uedono A, Onuma T, Sota T, Haskell B A, DenBaars S P, Speck J S, and Nakamura S 2005 *Appl. Phys. Lett.* **86** 021914.
[30] Koida T, Chichibu S F, Uedono A, Tsukazaki A, Kawasaki M, Sota T, Segawa Y, and Koinuma H 2003 *Appl. Phys. Lett*. **82** 532.
[31] For a review, see for example Krause-Rehberg R and Leipner H S 1999 *Positron Annihilation in Semiconductors, Solid-State Sciences* **127** (Berlin :Springer).
[32] Coleman P G 2000 *Positron Beams and Their Application* (Singapore :World Scientific) 1.
[33] Saarinen K, Laine T, Kuisma S, Nissilä J, Hautojärvi P, Dobrzynski L, Baranowski J M, Pakula K, Stepniewski R, Wojdak M, Wysmolek A, Suski T, Leszczynski M, Grzegory I, and Porowski S 1997 *Phys. Rev. Lett*. **79** 3030.
[34] Uedono A, Chichibu S F, Chen Z Q, Sumiya M, Suzuki R, Ohdaira T, Mikado T, Mukai T, and Nakamura S 2001 *J. Appl. Phys*. **90** 181.
[35] Uedono A, Koida T, Tsukazaki A, Kawasaki M, Chen Z Q, Chichibu S F, and Koinuma H 2003 *J. Appl. Phys*. **93** 2481.
[36] van Veen A, Schut H, Clement M, M. de Nijs J M, Kruseman A, and Ijpma M R 1995 *Appl. Surf. Sci*. **85** 216.
[37] Waltereit P, Brandt O, Trampert A, Grahn H T, Menniger J, Ramsteiner M, Reiche M, and Ploog K H 2000 *Nature* (London) **406** 865.
[38] Craven M D, Lim S H, Wu F, Speck J S, and DenBaars S P 2002 *Appl. Phys. Lett*. **81** 469.
[39] *Introduction to Nitride Semiconductor Blue Lasers and Light Emitting Diodes*, 2000, edited by S. Nakamura and S. F. Chichibu, (Taylor & Francis: London and New York).
[40] Wraback M, Shen H, Liang S, Gorla C R, and Lu Y 1999 *Appl. Phys. Lett*. **74** 507.
[41] Koida T, Chichibu S F, Uedono A, Sota T, Tsukazaki A, and Kawasaki M 2004 *Appl. Phys. Lett*. **84** 1079.
[42] Chichibu S F, Tsukazaki A, Kawasaki M, Tamura K, Segawa Y, Sota T, and Koinuma H 2002 *Appl. Phys. Lett*. **80** 2860.
[43] Chichibu S F, Sota T, Fons P J, Iwata K, Yamada A, Matsubara K, and Niki S 2002 *Jpn. J. Appl. Phys*. **41** L935.
[44] Muth J, Kolbas R, Sharma A, Oktyabrsy S, and Narayan J 1999 *J. Appl. Phys*. **85** 7884.
[45] Makino T, Chia C, Tuan N, Segawa Y, Kawasaki M, Ohtomo A, Tamura K, and Koinuma H 2000 *Appl. Phys. Lett*. **76** 3549.
[46] Look D C, Reynolds D C, Sizelove J R, Jones R L, Litton C W, Cantwell G, and Harsch W C 1998 *Solid State Commun*. **105** 399.
[47] Chichibu S F, Okumura H, Nakamura S, Feuillet G, Azuhata T, Sota T, and Yoshida S 1997 *Jpn. J. Appl. Phys*. **36** 1976.
[48] Cardona M 1969 *Modulation Spectroscopy, Solid State Phys. Suppl*. **11** ed S Seitz, D Turnbull, and H Ehrenreich (New York: Academic).
[49] Aspnes D E 1980 *Handbook on Semiconductors* ed T S Moss (Amsterdam: North-Holland) Vol. 2 Chap. 4A 109.
[50] Aspnes D E 1973 *Surf. Sci*. **37** 418.
[51] Gil B, Lusson A, Sallet V, Hassani S, Triboulet R, and Bigenwald P 2001 *Jpn. J. Appl. Phys*. **40** L1089.
[52] Thoma K, Dorner B, Duesing G, Wegener W 1974 *Solid State Commun*.**15** 1111.
[53] Chichibu S F, Torii K, Deguchi T, Sota T, Setoguchi A, Nakanishi H, Azuhata T, and Nakamura S 2000 *Appl. Phys. Lett*. **76** 1576.
[54] Torii K, Deguchi T, Sota T, Suzuki K, Chichibu S F, and Nakamura S 1999 *Phys. Rev*. B **60** 4723.

[55] Refractive index of ZnO at the B-exciton resonance wavelength (366.5 nm) is taken as 2.0 according to ref. 8 or Mollwo E 1954 *Angew. Phys.* **6** 257.
[56] Jellison Jr G E 1991 *J. Appl. Phys.* **69** 7627.
[57] Smith D and Baumeister P W 1979 *Appl. Opt.* **18** 111.
[58] Ghosh S, Waltereit P, Brandt O, Grahn H T, and Ploog K H 2002 *Phys. Rev*. B **65** 075202.
[59] Meyer B K, Alves H, Hofmann D M, Kriegseis W, Forster D, Bertram F, Christen J, Hoffmann A, Straßburg M, Dworzak M, Haboeck U, and Rodina A V 2004 *Phys. Stat. Sol*. (b) **241** 231.
[60] Tomzig E and Helbig R 1976 *J. Lumin*. **14** 403.
[61] Chakraborty A, Haskell B A, Speck J S, DenBaars S P, Nakamura S, and Mishra U K 2004 *Appl. Phys. Lett.* **85** 5143.
[62] Chichibu S F, Marchand H, Minski M S, Keller S, Fini P T, Ibbetson J P, Fleischer S B, Speck J S, Bowers J E, Hu E, Mishra U K, DenBaars S P, Deguchi T, Sota T, and Nakamura S 1999 *Appl. Phys. Lett*. **74** 1460.
[63] Nielsen B, Lymn K G, Vehanen A, and Schultz P J 1985 *Phys. Rev*. B **32** 7561.
[64] Uedono A, Wei L, Tabuki Y, Kondo H, Tanigawa S, Wada K, and Nakanishi H 1991 *Jpn. J. Appl. Phys*. **30** L2002.
[65] Sumiya M, Yoshimura K, Ohtsuka K, and Fuke S 2000 *Appl. Phys. Lett*. **76** 2098.

Report on **"Dielectric SiO_2/ZrO_2 distributed Bragg reflectors for ZnO microcavities prepared by reactive helicon-wave-excited-plasma sputtering and electron beam (e-beam) evaporation methods"**

Abstract

Distributed Bragg reflectors (DBRs) composed of multiple quarter-wavelength (λ/4) layers of SiO_2 and ZrO_2 were prepared by the home-made three-source e-beam (EB) evaporation system and reactive helicon-wave-excited-plasma sputtering (R-HWPS) methods, in order to obtain high-reflectivity (*R*) mirrors working at the resonance wavelength of B-excitons in ZnO (366.5 nm), which are necessary to fabricate cavity-coupled exciton-polariton laser structure, as shown in Fig. 4 of the preceding chapter. Especially, R-HWPS method was developed for the first time in this study. According to the surface-damage-free nature and better stoichiometry controllability of R-HWPS method, dense films exhibiting ideal refractive indices (1.46 for SiO_2 and 2.10 for ZrO_2 at 633 nm, being similar to the bulk values) having small RMS values for the surface roughness (0.20 nm for SiO_2 and 0.53 nm for ZrO_2) were deposited at room temperature using Si and Zr targets and O_2 gas. Optical reflectance spectra of the SiO_2/ZrO_2 DBRs agreed with those calculated using the optical multilayer film theory, and the 8-pair DBRs exhibited *R* higher than 99.5% at around 366.5 nm and the stop-band width (*R* >95%) as broad as 82 nm. The results indicate that R-HWPS is a suitable technique for the sputtering of insulating films, especially to fabricate the DBRs for the realization of polariton lasers using ZnO microcavities.

Introduction

In recent years, planar semiconductor microcavities (MCs) using distributed Bragg reflectors (DBRs) are attracting much attention because of the possibility in enhancing light-extraction efficiency of light-emitting-diodes and in realization of cavity-coupled exciton-polariton lasers, which are a coherent and monochromatic light source based on Bose condensation of the polaritons in MCs [1] in accordance with the strong light-matter coupling. The dispersion relation of exciton-polaritons forming upper and lower polariton branches (UPB and LPB, respectively) is shown schematically in the left-hand-side panel of Fig. 1. Longitudinal-transverse splitting of the exciton (ω_{LT}), which is the energy difference between the longitudinal and transverse excitons (ω_L and ω_T, respectively) at the wavevector k=0, represents the stability of exciton-polaritons. Once zero vector k is locked at the cavity-mode represented by the dotted line, the energy

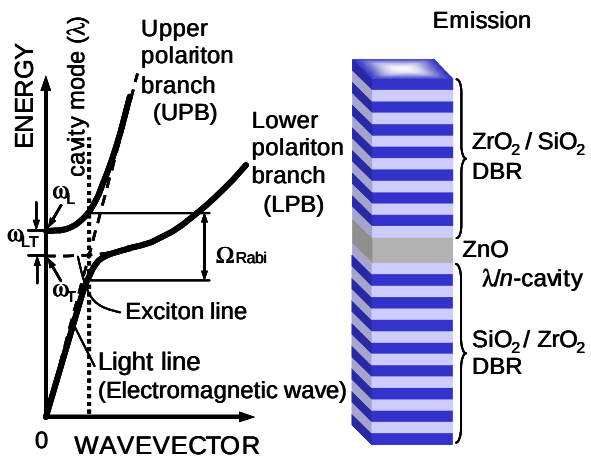

Fig. 1. Dispersion relation of exciton-polaritons (left-hand side) and a model ZnO MC consisted of ZnO λ/*n*-cavity sandwiched between 8 pairs of SiO_2/ZrO_2 and 7 pairs of ZrO_2/SiO_2 dielectric DBRs of λ/4*n* layers (right-hand side). Dashed lines show the dispersion of isolated excitons and light in the material. Longitudinal-transverse splitting of the exciton ω_{LT}, which is the energy difference between ω_L and ω_T at wavevector k=0, represents the stability of exciton-polaritons. Once k is locked at the dotted line, UPB and LPB is also locked and the vacuum field Rabi splitting Ω_{Rabi} has much larger value than the initial ω_{LT}.

difference between UPB and LPB (vacuum field Rabi splitting Ω_{Rabi}) becomes larger than the initial ω_{LT}, which indicate the enhanced coupling between the light and excitons. Bose condensation of the cavity polaritons can eventually be initiated by generating exciton-polaritons at the bottom of the lowest polariton branch at the k [1].

Since excitons in ZnO are stable at 300 K and ω_{LT} of the B-exciton has been reported to be as large as 11 meV [4-6], which is more than two orders of magnitude larger than that of GaAs being 0.08 meV, ZnO is of considerable interest for the room temperature operation of polariton lasers [7,8]. Indeed, Zamfirescu *et al*. [7] predicted a huge Ω_{Rabi} up to 120 meV for cavity polaritons in the model MC consisted of ZnO wavelength-cavity (λ/n-cavity, where n is the refractive index) sandwiched between $Mg_{0.3}Zn_{0.7}O$ / ZnO DBRs having 14 and 15 pairs of quarter-wavelength ($\lambda/4n$) layers in the top and bottom mirrors, respectively. The predicted Ω_{Rabi} value was later modified up to 191 meV (Ref. [8]), which is the record high value in semiconductor MCs, in the model MC consisted of ZnO λ/n-cavity with 7 and 8 pairs of ZrO_2/SiO_2 dielectric DBRs, as shown schematically in Fig. 1. The reason why the authors chose [8] SiO_2/ZrO_2 DBRs was that they are transparent for ultraviolet (UV) lights and the combination can realize high refractive index contrast that gives rise to high reflectivity (R) and wide stop-band width ($\Delta\lambda$), which is defined as the bandwidth for R>95%, even for small pair numbers N. Note that in the calculation in Ref. [8] and in this report, cavity photon mode was placed at 3.383 eV (366.5 nm) at zero detuning from the B-exciton resonance in ZnO and n of ZnO, SiO_2, and ZrO_2 at 366.5 nm were taken as 2.00 [7], 1.48 [9], and 2.10 [10], respectively. Corresponding layer thicknesses were 183.2, 61.9, and 44.7 nm for ZnO, SiO_2, and ZrO_2, respectively.

Because the gross R of DBRs is sensitive to the thickness and n of each layer and the interface sharpness, soft-deposition of very thin and flat dielectric films is mandatory. Dry processes such as electron-beam (EB) evaporation, ion-beam assisted deposition, plasma-enhanced chemical vapor deposition, and sputtering have usually been used to deposit dielectric films. Among these, sputtering can prepare large-area films of well-controlled compositions economically. Therefore, metals of high melting temperature, transparent conducting oxides (TCOs), and photovoltaic layer structures have been prepared by sputtering techniques. However, there are some essential problems such as resputtering and surface-damage caused by high energy sputtering particles. To overcome these problems, we have proposed [11] the use of helicon-wave-excited plasma (HWP), of which physics and experiments have been reported in the early 1990s [12-14], as a plasma source for the sputtering of thin films. The HWP can be excited remotely under relatively high vacuum ($\cong 10^{-2}$ Pa) producing a high density but low ion-energy plasma; the sputtering energy of Ar cations can be independently controlled by the target bias V_t. Accordingly, very smooth, highly [0001]-oriented, low-resistivity (5×10^{-4} Ω·cm) Al-doped ZnO (ZnO:Al) TCO films [11,15] and completely a-axis-locked (0001) ZnO and $Mg_xZn_{1-x}O$ epilayers [16] have been successfully grown according to the surface-damage-free nature; the technique was named *helicon-wave-excited-plasma sputtering* (HWPS) method. However, dielectric films have not yet been deposited by HWPS, since the V_t cannot be applied on the insulating targets such as SiO_2 or ZrO_2.

In this Chapter, development of *reactive* HWPS (R-HWPS) method is described to deposit SiO_2 and ZrO_2 dielectric films and their multilayer DBRs tuned at the resonance wavelength of B-excitons in ZnO, being suitable for ZnO microcavities. Dense and smooth single films and DBRs exhibiting R ≥99.5% at around 366.5 nm with $\Delta\lambda$= 82 nm were obtained by the room temperature deposition.

Experimental

A schematic representation of the HWPS system will be found elsewhere [11,16]. Approximately 100-nm-thick single films of SiO_2 and ZrO_2 as well as SiO_2/ZrO_2 DBR structures were deposited using a high purity undoped Si wafer and a 99.9%-pure undoped Zr metal as targets, which were placed on multi-target holders. The HWP excited in a quartz tube from the 99.9995%-pure Ar / 99.99995%-pure O_2 mixture with O_2 / (Ar + O_2) ratios between 0 and 0.6 was introduced into the chamber by the weak magnetic field gradient, and the velocity of Ar cations onto the target was accelerated by the negative dc V_t. Our configuration enables depositing thin films softly according to the elimination of plasma bombardment of the film surface, of which substrate was located off-axis from the azimuth connecting the center of the quartz tube and the target. The soda-lime-silica glasses and Si wafers were used as substrates. Typical rf power, V_t, and deposition pressure were 300 W, -400 V, and 0.2 Pa, respectively. The deposition was carried out at room temperature, and the substrate temperature was unintentionally increased to 90 °C. For comparison, SiO_2 and ZrO_2 single films and DBRs were deposited by EB evaporation using SiO_2 and ZrO_2 pellets.

Results and discussion

Single films of SiO_2 and ZrO_2 had a dense smooth surface with amorphous microstructures, as shown in the atomic-force-microscopy (AFM) images on the left-hand-side panels of Figs. 2(a) and 2(b), respectively, while those of the films prepared by EB evaporation exhibited granular structures (right-hand side panels). The surface morphology, flatness, and n of each film were strongly influenced by $O_2/(Ar+O_2)$. The RMS surface roughness took the smallest values for $O_2/(Ar+O_2)$=0.25, namely 0.2 nm for SiO_2 and 0.53 nm for ZrO_2. They are smaller than those of the films deposited by EB evaporation (0.47 nm for SiO_2 and 1.37 nm for ZrO_2). Values of n for the best films were measured by an ellipsometry at 633 nm to be 1.46 for SiO_2 and 2.10 for ZrO_2, which agreed with those of the bulk SiO_2 (Ref. [9]) and ZrO_2 (Ref. [10]). The RMS roughness increased and the amorphous grain size decreased with increasing $O_2/(Ar+O_2)$ greater than 0.25, indicating the importance of gas phase and hence solid phase stoichiometry. Simultaneously, n of the films tended to decrease with $O_2/(Ar+O_2)$. The results indicate that n is connected with the film packing density; high n can be obtained for

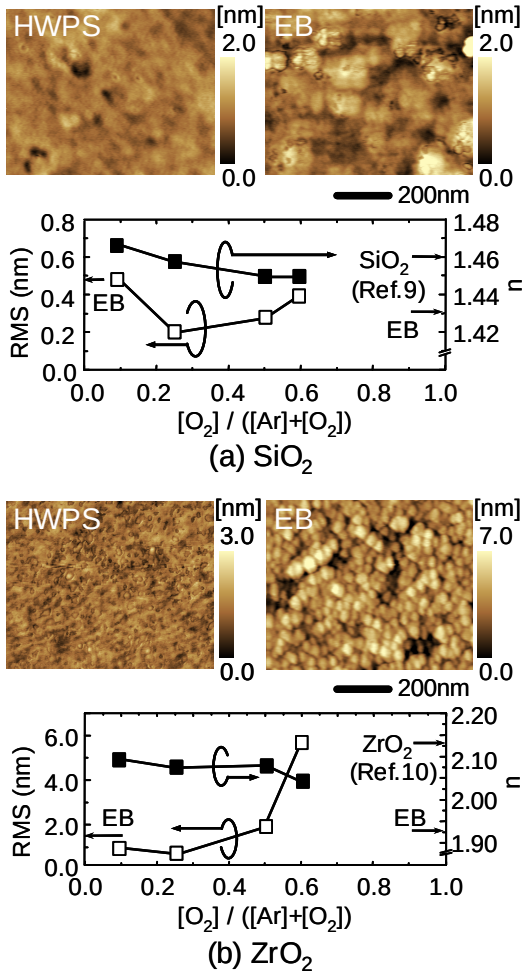

Fig. 2 Representative AFM images of (a) SiO_2 and (b) ZrO_2 films deposited by R-HWPS for $O_2/(Ar+O_2)$=0.25. For comparison, those of the films deposited by EB evaporation are shown in the right-hand side panels. The RMS values of the surface roughness and refractive indices n of (a) SiO_2 and (b) ZrO_2 films are plotted as a function of $O_2/(Ar+O_2)$. Corresponding values of the bulk SiO_2 and ZrO_2 and those of the films prepared by EB evaporation are indicated by arrows on the vertical axes for comparison.

dense films having less porous character [17]. As a matter of fact, *n* of the films deposited by EB evaporation (1.43 for SiO_2 and 1.93 for ZrO_2) were far smaller than the bulk value.

The improvements in the film properties using R-HWPS compared to EB evaporation are due to the reactive (surface-damage-free) nature and better stoichiometry controllability, as follows. In case of EB evaporation, SiO_x or ZrO_x molecules and/or clusters are evaporated by the EB bombardment of SiO_2 or ZrO_2 pellet. Because the molecules / clusters hardly migrate on the surface, the resultant films in general have granular structure. Conversely, excited neutral Si^* or Zr^* as well as atomic one can be sputtered by the HWP accelerated by V_t and they react with O_2 at the surface after proper migration for R-HWPS, resulting in the smooth surface. The generation of excited atomic species during HWPS have been evidenced from the plume emission spectra of ZnO and MgZnO targets [16], in which the film growth rate increased linearly with Zn^* and Mg^* emission intensity. The separate feeding of Si (or Zr) and O_2 eventually enables precise stoichiometry control. The unwanted increase in the RMS roughness value for $O_2/(Ar+O_2) \geq 0.5$ is considered to be due to the molecule formation owing to the O_2 overpressure (nonstoichiometry).

Normal-incidence optical reflectance (OR) spectra of the model SiO_2/ZrO_2 DBRs were calculated as a function of *N* by the optical multilayer film equations [18] using the values listed above. Note that *n* values of SiO_2 and ZrO_2 used for the calculation were measured as a function of λ by the spectroscopic ellipsometry using the single films deposited on Si substrates. The result for *N*=8 is shown by the dotted line in Fig. 3. Also, calculated *R* at 366.5 nm and Δλ are shown as a function of *N* in the inset. As shown, *R* higher than 99.5% and Δλ=63.9 nm were obtained for *N*=8, predicting the high performance of the model dielectric DBRs.

Normal-incidence OR spectra of the DBRs were measured at 293 K using a white light from a Xe lamp. Reflected light was dispersed by a grating monochromator and detected using a charge-coupled device array, where the absolute *R* values were carefully calibrated using the Al mirror. The OR spectra of 8-pair SiO_2/ZrO_2 DBRs deposited by R-HWPS and EB evaporation nearly agreed with the calculated one, as shown by red and black lines in Fig. 3, respectively. The DBR deposited by R-HWPS exhibited very high *R* higher than 99.5% at around 366.5 nm. However, its central λ was approximately 360 nm and Δλ was 82 nm, the latter being 18 nm wider than the calculated value. In addition, *R* minima in the side fringes did not reach zero. These deviations are considered to be due to the considerable variation in the optical thickness of the layers arising from fluctuations in actual thickness and higher index contrast between SiO_2 and ZrO_2 layers. Nevertheless, maximum *R* was higher and Δλ was wider than those of the DBR deposited by EB evaporation, the results indicate the superior performance

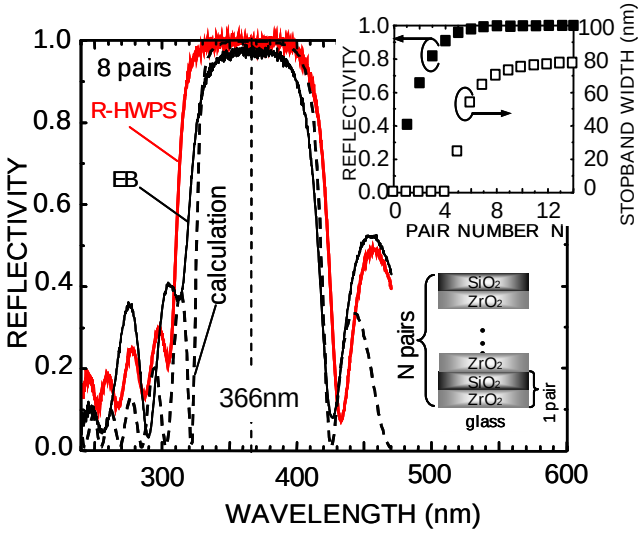

Fig. 3 Theoretically calculated OR spectrum of the model 8-pair SiO_2/ZrO_2 DBR (dotted line) and measured OR spectra of the 8-pair SiO_2/ZrO_2 DBRs deposited by R-HWPS (thick solid line) and EB evaporation (thin solid line). The inset shows the reflectivity *R* at 366.5 nm and Δλ, which is defined as the bandwidth having *R* higher than 95%, as a function of pair number *N*.

of R-HWPS method in terms of higher packing density, higher index contrast, and sharper heterointerfaces.

Conclusion

In summary, R-HWPS method was developed to fabricate SiO_2/ ZrO_2 dielectric DBRs suitable for the use in ZnO MCs operating at 366-nm UV lights. According to the surface-damage-free nature and better stoichiometry controllability, dense and smooth SiO_2 and ZrO_2 films exhibiting ideal *n* values were successfully deposited at room temperature. The 8-pair DBR exhibited *R* higher than 99.5% and 82-nm-bandwidth. Since high-quality ZnO and MgZnO epilayers and ZnO:Al TCO films have already been grown using HWPS method, present achievements may enable to fabricate the MC structures without ever exposing the interfaces in air.

References

[1] F. Tassone, C. Piermarocchi, V. Savona, A. Quattropani, and P. Schwendimann, Phys. Rev. B **56**, 7554 (1997); G. Malpuech, A. Kavokin, A. Di Carlo, and J. J. Baumberg, *ibid* **65**, 153310 (2002).

[2] C. Weisbuch, M. Nishioka, A. Ishikawa, and Y. Arakawa, Phys. Rev. Lett. **69**, 3314 (1992).

[3] A. Imamoglu, R. J. Ram, S. Pau, Y. Yamamoto, Phys. Rev. A **53**, 4250 (1996).

[4] K. Hummer and P. Gebhardt, Phys. Status Solidi (b) **85**, 271 (1978).

[5] J. Lagois, Phys. Rev. B **23**, 5511 (1981).

[6] S. F. Chichibu, T. Sota, G. Cantwell, D. B. Eason, and C. W. Litton, J. Appl. Phys. **93**, 756 (2003).

[7] M. Zamfirescu, A. Kavokin, B. Gil, G. Malpuech, and M. Kaliteevski, Phys. Rev. B **65**, 161205R (2002).

[8] S. F. Chichibu, A. Uedono, A. Tsukazaki, T. Onuma, M. Zamfirescu, A. Ohtomo, A. Kavokin, G. Cantwell, C. W. Litton, T. Sota, and M. Kawasaki, Semicond. Sci. Technol. **20**, S67 (2005).

[9] G. E. Jellison, Jr., J. Appl. Phys. **69**, 7627 (1991).

[10] C. West, *CRC Handbook of Chemistry and Physics*, (CRC Press, Boca Raton, FL, 1984).

[11] K. Yamaya, Y. Yamaki, H. Nakanishi, and S. Chichibu, Appl. Phys. Lett. **72**, 235 (1998).

[12] F. Chen, Plasma Phys. and Controlled Fusion, **33**, 339 (1991); J. Vac. Sci. Technol. A **10**, 1389 (1992).

[13] R. Boswell, *Proc. of 21st Int'l Conf. on Phenomena in Ionised Gases*, eds. G. Ecker, U. Arendt, J. Boseler, and A. Brunn (Arbeitsgemeinschaft Plasma Physik, Bochum, 1993), pp.18.

[14] T. Nakano, K. Giapis, R. Gottscho, T. Lee, and N. Sadeghi, J. Vac. Sci. Technol. B **11**, 2046 (1993).

[15] S. F. Chichibu, T. Ohmori, N. Shibata, T. Koyama, and T. Onuma, Appl. Phys. Lett. **85**, 4403 (2004).

[16] S. F. Chichibu, T. Yoshida, T. Onuma, and H. Nakanishi, J. Appl. Phys. **91**, 874 (2002); T. Koyama, T. Onuma, and S. F. Chichibu, Appl. Phys. Lett. **83**, 2973 (2003); T. Koyama and S. F. Chichibu, J. Appl. Phys. **95**, 7856 (2004); T. Koyama, T. Ohmori, N. Shibata, T. Onuma, and S. F. Chichibu, J. Vac. Sci. Technol. B **22**, 2220 (2004).

[17] for example, see M. Rothschild, D. J. Ehrlich, and D. C. Shaver, Appl. Phys. Lett. **55**, 1276 (1989); E. N. Glezer and E. Mazur, Appl. Phys. Lett. **71**, 882 (1997).

[18] for example, see S. Fujihara, K. Ishiguro, H. Ikeda, and H. Yokota, *Optical Thin Films* (Kyoritsu, Tokyo, 1985); X. Wang, H. Masumoto, Y. Someno, and T. Hirai, J. Vac. Sci. Technol. A **17**, 206 (1999).

Report on **"Strain-relaxation in NH_3-source molecular beam epitaxy of AlN epilayers on GaN/Al_2O_3 epitaxial templates prepared by MOVPE"**

Abstract

As the first step to fabricate AlGaN/AlGaN heterostructures for our DBR, AlN films were grown by NH_3-MBE on the GaN/Al_2O_3 epitaxial templates prepared by MOVPE. Temporal evolution of surface morphology in AlN epilayers grown by NH_3-source molecular beam epitaxy on the GaN / (0001) Al_2O_3 epitaxial templates was correlated with changes in sign and degree of the residual strain by increasing the layer thickness. They began to crack for the thickness as thin as 10 nm. However, atomic-layer step-and-terrace surface structures were maintained for the thickness up to 32 nm. Tensile biaxial stress decreased with further increase in the thickness due to the lattice relaxation, which caused surface roughening. An 1580-nm-thick, nearly strain-compensated AlN epilayer, of which threading dislocation density was reduced down to $5x10^9$ cm^{-2}, exhibited excitonic photoluminescence peaks at 6.002 and 6.023 eV at 9 K and a near-band-edge peak at 5.872 eV at 293 K. We will grow AlN/AlGaN or AlGaN/AlGaN DBRs in the future.

Introduction

One of the merits of molecular beam epitaxy (MBE) over metalorganic vapor phase epitaxy (MOVPE) is the possible preparation of atomically abrupt heterointerfaces, which is really important for the DBR application we are investigating. Efforts to make use of advantages of both MBE and MOVPE enabled to obtain a record high two-dimensional electron gas mobility in $Al_xGa_{1-x}N$ / GaN heterostructures [1] and to fabricate $In_xGa_{1-x}N$ / GaN quantum well light emitting diodes and laser diodes [2]: those heterostructures were grown by MBE on GaN / (0001) Al_2O_3 epitaxial templates prepared by MOVPE. Recently, proper feeding of NH_3 flux and the insertion of flux-modulated GaN (FM-GaN), in which Ga flux was supplied intermittently during heating the GaN templates up to the growth temperature (Tg=800°C), have been shown to improve the surface morphology, Hall mobility, and photoluminescence (PL) qualities of GaN homoepitaxial layers grown by NH_3-source MBE (NH_3-MBE) [3]. However, surface crevices originating from dislocation pits of the GaN templates yet remained. In order to eliminate them, the use of an AlN layer grown at high-temperature (HT-AlN) must be effective, since the density of both the edge- and screw-type threading dislocations (TDs) in GaN overlayers has been shown to decrease by the use of HT-AlN [4, 5]. Also, the growth of crack-free AlN on GaN may enable to fabricate quantum heterostructure devices having large band offsets.

In this Chapter, strain states and their influence on the surface morphology of HT-AlN grown by NH_3-MBE on the GaN / (0001) Al_2O_3 templates are discussed as a function of HT-AlN thickness. The residual strain changed from tensile to compressive with increasing the thickness due to the lattice relaxation, and the disappearance of surface atomic-layer step-and-terrace structures was attributed to the introduction of cracks. Nevertheless, an 1580-nm-thick AlN, of which threading dislocation density was reduced down to $5x10^9$ cm^{-2}, exhibited an excitonic PL peak at 6.002 eV with a shoulder at 6.023 eV at 9 K and a near-band-edge (NBE) peak at 5.872 eV at 293 K.

Experiment

Approximately 10- to 1580-nm-thick HT-AlN were grown by NH_3-MBE on 1400-nm-thick undoped GaN templates prepared by MOVPE. The templates had an atomically flat surface with one monolayer (ML)-high step-and-terrace structures, as shown in Fig. 1(a). The TD density (TDD) near the surface was approximately 10^9 cm^{-2} (TEM result will be shown later). The

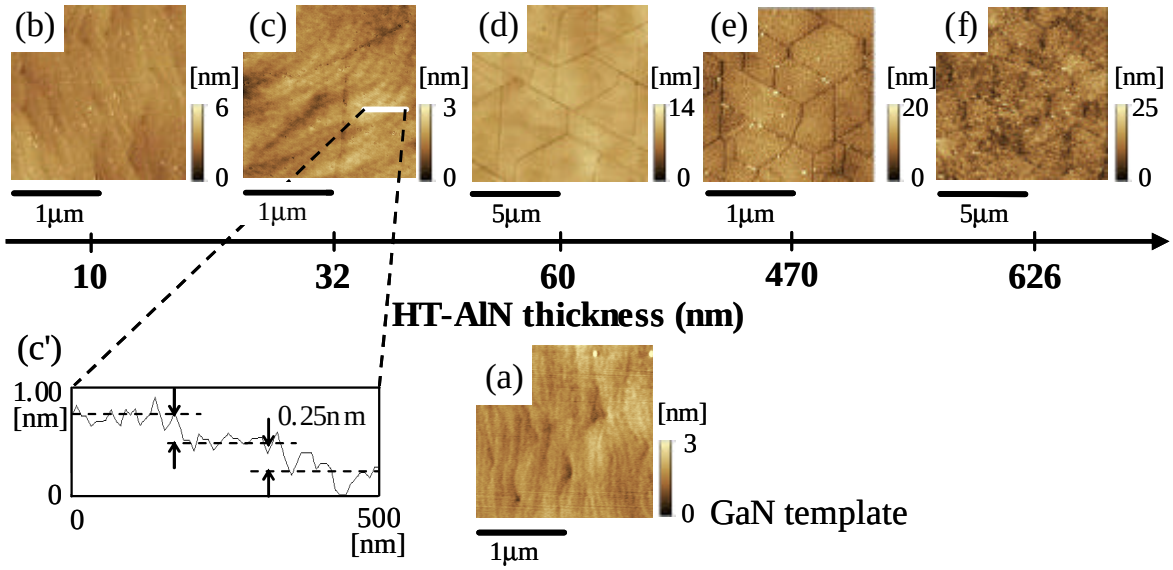

Fig. 1. AFM images of the surface of (a) GaN / (0001) Al_2O_3 epitaxial template and those for (b) 10-nm, (c) 32-nm, (d) 60-nm, (e) 470-nm, and (f) 626-nm-thick HT-AlN. (c') A cross-sectional height profile of the 32-nm-thick HT-AlN is also shown; the 0.25-nm step height corresponds to a half of the c-lattice parameter [7].

growth was initiated with 2- to 6-ML-thick AlN deposition at 550 °C (LT-AlN), followed by the HT-AlN growth at 830 °C using a metallic Al and an uncracked NH_3 gas. The growth pressure was kept between 9×10^{-6} and 3×10^{-5} Torr, while the base pressure was lower than 1×10^{-9} Torr. The Al beam equivalent pressure and NH_3 flow rate were 2.3×10^{-7} Torr and 60-100 sccm, respectively. The typical growth rate was 375 nm/h.

Results and discussion

Atomic-force microscopy (AFM) images of HT-AlN are shown in Figs. 1(b)-1(f) as a function of the layer thickness. The surface flatness as well as step-and-terrace structures were maintained for the layers thinner than 32 nm, as shown in Figs. 1(b), 1(c), and 1(c'). The results indicate that a few-ML-thick LT-AlN functioned as an wetting layer [6] as well as a decomposition-shielding layer for the GaN templates, as is the case with FM-GaN [3]. The value of RMS roughness of those HT-AlN was as small as 0.51 nm, which nearly corresponds to 2 MLs [7]. However, as expected from extremely thin critical thickness of AlN on GaN (0.5~0.75 nm) [8, 9], certain precursors of cracks were already formed as microscopic pits aligned along [1-100] directions, as shown in Figs. 1(b) and 1(c). They developed into distinct cracks having a hexagonal network with an average spacing of 1-2 μm, as shown in Fig. 1(d). With further increase in the thickness, three-dimensional (3D) nuclei appeared between the cracks, and finally they formed 3D domains, as shown in Figs. 1(e) and 1(f).

These morphological evolution is correlated with the residual strain, as follows. As shown in the 2θ-ω x-ray diffraction (XRD) patterns in Fig. 2(a), the intensity of the (0002) AlN diffraction peak increased and the value of full width at half maximum (FWHM) decreased to 150 s with the increase in thickness from 10 to 1580 nm. The change in the FWHM value is explained by the Sherrer's limit for the films thinner than 100 nm (data plot not shown). To visualize the strain evolution in HT-AlN, the *c*-lattice parameter, which was calculated from the position of (0002) diffraction peak, is plotted as a function of thickness in Fig. 2(b). For comparison, the value of

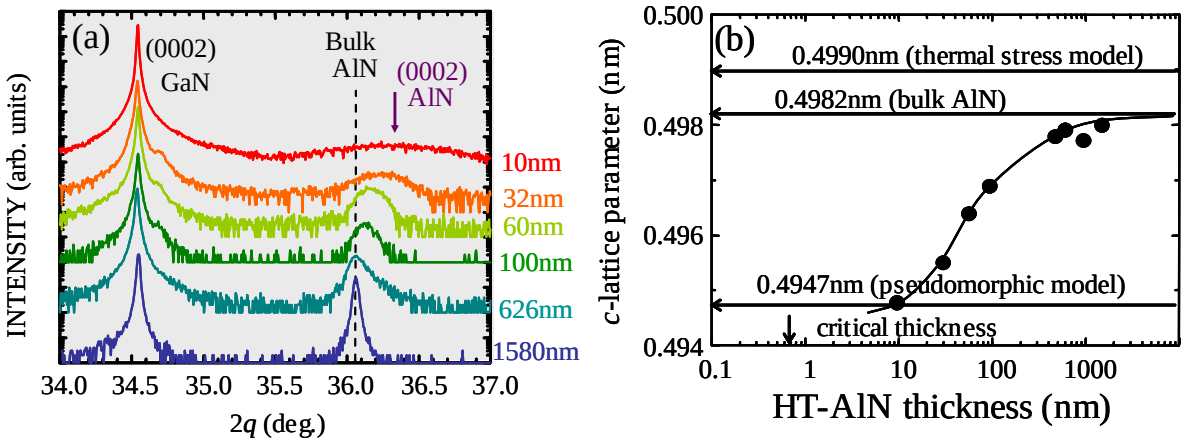

Fig. 2. (a) 2θ-ω XRD patterns and (b) *c*-lattice parameters of HT-AlN grown on the GaN templates as a function of HT-AlN thickness. The horizontal arrows in (b) show the *c*-lattice parameters of bulk AlN [7] and strained epilayers according to the pseudomorphic model and thermal stress model [10, 11]. The vertical arrow shows a critical thickness in the AlN / GaN heteroepitaxy.

bulk AlN (0.4982 nm) [7] and those of strained AlN epilayers calculated according to [10, 11] the pseudomorphic model (0.4947 nm) and thermal stress model (0.4990 nm) are shown by horizontal arrows. In the former model, the in-plane *a*-lattice parameter was set equal to that of the GaN template and *c*-lattice parameter was calculated based on the quasi-cubic approximation, $\varepsilon_{zz}=-2(C_{13}/C_{33})\varepsilon_{xx}$, where ε_{zz} and ε_{xx} are out-plane and in-plane strains, respectively, and C_{13} and C_{33} are the elastic stiffness constants [12]. In the latter model, epilayer was assumed to be fully relaxed at T_g and elastically strained during cooling due to the difference of thermal expansion coefficients [13, 14] between AlN and Al_2O_3. As shown, the pseudomorphic tensile biaxial stress partly remained for HT-AlN thinner than approximately 1000 nm. However, the stress decreased with increasing thickness due to the gradual lattice relaxation, which is considered to be the source of pits, cracks, and 3D growth observed in Fig. 1. Note that the lattice mismatch between GaN and AlN is as large as 2.3 %, and the 1580-nm-thick HT-AlN is considered to be mostly relaxed at T_g, as is the case with the 1-μm-thick AlN / (0001) Al_2O_3 grown by MOVPE [15].

The symmetric (0002) AlN and asymmetric (10-12) AlN XRD ω-rocking curves of the 1580-nm-thick, nearly strain-compensated HT-AlN on the GaN template are shown in Fig. 3(a).

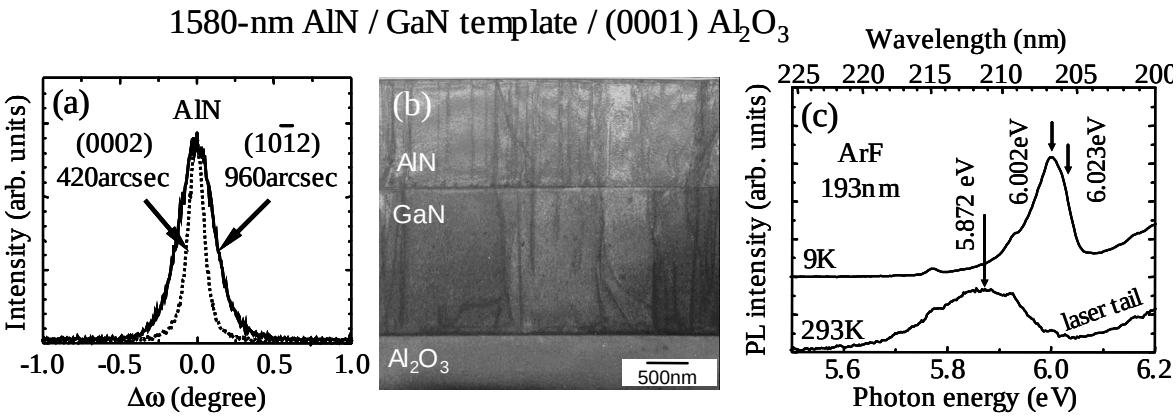

Fig. 3. (a) (0002) AlN and (10-12) AlN XRD ω-rocking curves, (b) cross-sectional TEM image, and (c) PL spectra measured at 9 K and 293 K of the 1580-nm-thick HT-AlN epilayer on GaN/Al_2O_3 epitaxial template. The increase of the PL intensity higher than 6.1 eV is due to the scattering of the 193 nm line of an ArF excimer laser.

The FWHM values were 420 s and 960 s, respectively, indicating the presence of predominantly edge-component and certain screw-component TDs [16]. Values of TDD near the surface regions of HT-AlN and GaN template were estimated by transmission electron microscopy to be 6×10^9 and 2×10^9 cm^{-2}, respectively, as shown in Fig. 3(b). The former value is lower than that of the AlN epilayer directly grown on (0001) Al_2O_3 by MOVPE being 1×10^{10} cm^{-2} [15], and the result encourages to grow low TDD GaN overlayers. PL spectra of the same sample excited by the 193 nm line of an ArF excimer laser (5 mJ, defocused) are shown in Fig. 3(c). The spectrum measured at 9 K exhibited an excitonic [17] PL peak at 6.002 eV with a shoulder at 6.023 eV. The energies are close to that of the major cathodoluminescence peak at 77 K (6.052 eV) [18] of the compressively-strained AlN / (0001) Al_2O_3 grown by MOVPE [15]. The NBE peak was also observed at 5.872 eV (211.1 nm) at 293 K, indicating certainly low density of nonradiative recombination channels. The achievement of low TDD HT-AlN exhibiting NBE deep ultraviolet (211.1 nm) PL peak at room temperature encourages one to grow high quality AlN layers for 2D GaN- and AlGaN-based heterostructures by NH_3-MBE.

Conclusion

The atomic-layer step-and-terrace surface structures were obtained for the AlN epilayers thinner than 32 nm, which were grown by NH_3-MBE on the GaN / (0001) Al_2O_3 epitaxial templates. The residual tensile strain in HT-AlN decreased with the increase in the layer thickness due to the lattice relaxation, and the surface morphology simultaneously degraded due to the formation of pits, cracks, and 3D nuclei. Nevertheless, nearly strain-compensated 1580-nm-thick AlN, of which TDD was reduced down to $5x10^9$ cm^{-2}, exhibited an excitonic PL peak at 6.002 eV with a shoulder at 6.023 eV at 9 K, and a NBE peak at 5.872 eV at 293 K. We are going to prepare AlN/AlGaN or AlGaN/AlGaN DBR in the near future.

References

[1] C. R. Elsass, I. P. Smorchkova, B. Heying, E. Haus, P. Fini, K. Maranowski, J. P. Ibbetson, S. Keller, P. M. Petroff, S. P. DenBaars, and U. K. Mishra, Appl. Phys. Lett. **74**, 3528 (1999).

[2] S. E. Hooper, M. Kauer, V. Bousquet, K. Johnson, J. M. Barnes, and J. Heffernan, Electron. Lett. **40**, 33 (2004); S. E. Hooper, M. Kauer, V. Bousquet, K. Johnson, C. Zellweger, and J. Heffernan, J. Cryst. Grwoth **278**, 361 (2005).

[3] T. Koida, Y. Uchinuma, J. Kikuchi, K. R. Wang, M. Terazaki, T. Onuma, J. F. Kaeding, R. Sharma, S. Naka-mura, and S. F. Chichibu, J. Vac. Sci. Technol. B **22**, 2158 (2004).

[4] K. Kusakabe, K. Kishino, A. Kikuchi, T. Yamada, D. Sugihara, and S. Nakamura, J. Cryst. Growth **230**, 387 (2001).

[5] M. Sakai, H. Ishikawa, T. Egawa, T. Jimbo, M. Umeno, T. Shibata, K. Asai, S. Sumiya, Y. Kuraoka, M. Tanaka, and O. Oda, J. Cryst. Growth **244**, 6 (2002).

[6] S. Yoshida, S. Misawa, and S. Gonda, Appl. Phys. Lett. **42**, 427 (1983).

[7] W. M. Yim, E. J. Stofko, P. J. Zanzucchi, J. I. Pankove, M. Ettenberg, and S. L. Gilbert, J. Appl. Phys. **44**, 292 (1973).

[8] J. W. Matthews, J. Vac. Sci. Technol. **12**, 126 (1975).

[9] A. D. Bykhovski, B. L. Gelmont, and M. S. Shur, J. Appl. Phys. **78**, 3691 (1995).

[10] K. Hara, T. Shinozawa, J. Yoshino, and H. Kukimoto, Jpn. J. Appl. Phys. **30**, L437 (1991).

[11] S. Chichibu, S. Shirakata, M. Uchida, Y. Harada, T. Wakiyama, S. Matsumoto, H. Higuchi, and S. Isomura, Jpn. J. Appl. Phys., Part 1 **34**, 3991 (1995).

[12] K. Shimada, T. Sota, and K. Suzuki, J. Appl. Phys. **84**, 4951 (1998).

[13] H. P. Maruska and J. J. Tietjen, Appl. Phys. Lett. **15**, 327 (1969).
[14] W. M. Yim and R. J. Paff, J. Appl. Phys. **45**, 1456 (1974).
[15] T. Shibata, K. Asai, T. Nagai, S. Sumiya, M. Tanaka, O. Oda, H. Miyake, and K. Hiramatsu, Mat. Res. Soc. Symp. Proc. **693**, 541 (2002); T. Shibata, K. Asai, S. Sumiya, M. Mouri, M. Tanaka, O. Oda, H. Katsukawa, H. Miyake, and K. Hiramatsu, Phys. Stat. sol. (c) **0**, 2023 (2003).
[16] B. Heying, X. H. Wu, S. Keller, Y. Li, D. Kapolnek, B. P. Keller, S. P. DenBaars, and J. S. Speck, Appl. Phys. Lett. **68**, 643 (1996).
[17] E. Silveira, J. A. Freitas, Jr., O. J. Glembocki, G. A. Slack, and L. J. Schowalter, Phys. Rev. B **71**, 041201 (2005).
[18] T. Onuma, S. F. Chichibu, T. Sota, K. Asai, S. Sumiya, T. Shibata, and M. Tanaka, Appl. Phys. Lett. **81**, 652 (2002).